



Linear stability of a falling film over a heated slippery planeArnab Choudhury  and Arghya Samanta ^{*}*Department of Applied Mechanics, Indian Institute of Technology Delhi, 110016 Delhi, India*

(Received 3 April 2022; accepted 5 June 2022; published 28 June 2022)

A detailed parametric study on the linear stability analysis of a three-dimensional thin liquid film flowing down a uniformly heated slippery inclined plane is carried out for disturbances of arbitrary wavenumbers, where the liquid film satisfies Newton's law of cooling at the film surface. A coupled system of boundary value problems is formulated in terms of the amplitudes of perturbation normal velocity and perturbation temperature, respectively. Analytical solution of the boundary value problems demonstrates the existence of three dominant modes, the so-called H mode, S mode, and P mode, where the S mode and P mode emerge due to the thermocapillary effect. It is found that the onset of instabilities for the H mode, S mode, and P mode reduces in the presence of wall slip and leads to a destabilizing influence. Numerical solution based on the Chebyshev spectral collocation method unveils that the finite wavenumber H-mode instability can be stabilized, but the S-mode instability and the finite wavenumber P-mode instability can be destabilized by increasing the value of the Marangoni number. On the other hand, the Biot number shows a dual role in the H-mode and S-mode instabilities. But the P-mode instability can be made stable with the increasing value of the Biot number and the decreasing values of the Marangoni number and the Prandtl number. Furthermore, the H-mode and S-mode instabilities become weaker, but the P-mode instability becomes stronger, with the increasing value of the spanwise wavenumber. In addition, the shear mode emerges in the numerical simulation when the Reynolds number is large, which can be destabilized slightly with the increasing value of the Marangoni number; however, it can be stabilized with the increasing value of the slip length and introducing the spanwise wavenumber to the infinitesimal perturbation.

DOI: [10.1103/PhysRevE.105.065112](https://doi.org/10.1103/PhysRevE.105.065112)**I. INTRODUCTION**

The studies of interfacial heat transfer and stability of thin liquid films have grabbed the attention of many researchers worldwide due to their widespread applications in engineering and science. In several types of industrial equipment, such as falling film evaporators, condensers, etc., thin liquid films are often encountered because of their large contact area and small thermal resistance [1]. Furthermore, the heat and mass transfer rates on the surface of a thin liquid film enhance significantly due to the solitary wave formation, as reported by Frisk and Davis [2] and Brauner and Maron [3]. In addition, for the cooling of microelectronic devices and thermal protection of rocket engines, thin liquid films are also used. Besides these engineering applications, due to the importance of fundamental problems in heat transfer and fluid mechanics, the study of a heated falling film has its own relevance because the heat transfer at the film surface plays a major role in the surface wave dynamics developed under the action of gravitational force.

The studies of linear and nonlinear stability analyses of an isothermal thin liquid falling film have been accomplished extensively after the pioneering experiment of Kapitza and Kapitza [4], where all the events starting from the initiation of instability to the formation of a large teardrop-shaped solitary wave have been shown (see, for example, Alekseenko *et al.*

[5], Chang [6], Liu and Gollub [7], and Craster and Matar [8]). In this context, the linear stability of an isothermal thin liquid film falling under the action of gravitational force had been analyzed by both Benjamin [9] and Yih [10] for the flow at a low Reynolds number. The Orr-Sommerfeld eigenvalue problem was formulated, and the surface mode or H mode was identified by using the long-wave asymptotic expansion, where it was assumed that the wavelength of the infinitesimal disturbance is very large compared to the liquid film thickness. The critical Reynolds number for the H mode was also expressed as a function of inclination angle beyond which the liquid film flow becomes unstable. The existence of shear mode for the isothermal gravity-driven falling liquid film was found by Lin [11], Bruin [12], and Chin *et al.* [13] at the higher values of the Reynolds number. Bruin's result indicated that both surface and shear modes compete with each other for initiating the primary instability when the inclination angle is very low. Later, Floryan *et al.* [14] explored the effect of surface tension on the shear mode for an isothermal falling liquid film.

In parallel, in the context of a thermocapillary instability, Lin [15] performed a linear stability analysis of a thin liquid film falling down a heated inclined plane by using the long-wave asymptotic expansion in the low Reynolds number regime. The critical Reynolds number for the H mode beyond which the flow becomes unstable was calculated analytically and expressed as a function of inclination angle, Marangoni number, and other flow parameters. Later, Sreenivasan and Lin [16] revisited the above study on exploring the

^{*}arghya@am.iitd.ac.in

thermocapillary instability in an arbitrary wavenumber regime when the inclination angle is sufficiently small. Smith [17] investigated the effect of Prandtl number on the primary instability of a heated falling liquid film in the long-wave regime. He pointed out that the flow may become unstable at the higher values of Prandtl number due to heating or cooling of the plane. He also provided a physical mechanism for the initiation of primary instability. Goussis and Kelly [18] carried out a detailed energy budget analysis for a falling liquid film over a uniformly heated substrate to figure out the physical mechanism of primary instability. In fact, they proposed three mechanisms by which the instability can initiate. They recognized two thermocapillary modes (S mode and P mode) and one hydrodynamic mode (H mode) in low to moderate values of the Reynolds number, where the hydrodynamic mode (H mode) and one thermocapillary mode (S mode) emerge in the long-wave regime while the other thermocapillary mode (P mode) emerges in the short-wave regime. The effects of Marangoni number on these three individual modes were explored, and their results revealed that the Marangoni number has a destabilizing influence on the long-wave H mode and S mode, as well as the short-wave P mode. Joo *et al.* [19] accomplished a linear stability analysis of a heated falling liquid film with the aid of the long-wave asymptotic expansion, where they considered the evaporation effect on the thermocapillary instability. Later, Joo *et al.* [20] further extended their previous study to decipher the nonlinear stability induced by the H mode based on the evolution equation for the liquid film thickness. They reported that the rivulet formation is responsible for the thermocapillary S-mode instability. Ruyer-Quil *et al.* [21] and Scheid *et al.* [22] studied the instability of a heated liquid film falling down an inclined plane in detail to decipher the complex wave dynamics on the surface of a liquid film under the framework of the low-dimensional model, where the evolution equations were formulated for the local film thickness, local flow rate, and mean temperature across the layer, and computed the steady state traveling wave solution. They demonstrated that the results obtained from the linear stability analysis of the model equations are in good agreement with that of the Orr-Sommerfeld boundary value problem. They also identified the hydrodynamic H-mode and the thermocapillary S-mode instabilities. It was reported that the hydrodynamic H-mode and the thermocapillary S-mode instabilities reinforce each other with the increase in the value of the Marangoni number. Hu *et al.* [23] performed a linear stability analysis of a binary liquid film falling down a heated inclined plane. The effect of Soret number on the three individual modes (H, S, and P modes) had been discussed for low to moderate values of the Reynolds number, where the Soret number was found to have a destabilizing effect on the unstable modes, similar to that observed for the Marangoni number. Furthermore, it was revealed that the H mode and S mode merge with each other at the higher values of the Soret number. The variation of P mode with the Soret number was captured partially up to the moderate value of the Reynolds number. The absolute and convective instabilities were also investigated in their study. Samanta [24] analyzed the effects of Marangoni number and Biot number on the temporal instability for an inertialess liquid film flowing down a uniformly heated wall. His result indicated a destabilizing effect of the

Biot number on the temporal mode. A nonlinear stability analysis of a heated liquid film flowing down an inclined plane was performed by Dávalos-Orozco [25] based on the Benney-type surface evolution equation, where the effects of wall thickness and heat conductivity on the instability had been deciphered. Some significant results regarding the instability of thin liquid films flowing down isothermal and nonisothermal inclined substrates can be found in the review paper of Dávalos-Orozco [26].

It is observed that for many flows occurring in nature as well as encountered in engineering applications, the no-slip condition is not valid at the liquid-solid interface [27,28]. Rather, in such situations, the velocity field satisfies the Navier-slip boundary condition appropriately at the liquid-solid interface. The Navier-slip boundary condition may also be implemented at the liquid-solid interface to model a liquid film flowing over a permeable substrate when the superficial volume average velocity of liquid in the porous medium is small compared to the velocity of liquid in the liquid medium as demonstrated by Pascal [29]. Although the existence of a Navier-slip-type empirical boundary condition was initially proposed by Beavers and Joseph [30], which was theoretically justified by Saffman [31]. Samanta *et al.* [32] carried out linear and nonlinear stability analyses in detail for a liquid film falling down a slippery inclined plane. Their result indicated that the slip length has a destabilizing effect on the surface mode or H mode in the low Reynolds number regime, i.e., near the criticality. However, it showed a stabilizing effect in the moderate Reynolds number regime. In the presence of wall slip, they have also revealed the amplification of speed and amplitude of the traveling wave solution. After that, Ding and Wong [33] extended the model of Samanta *et al.* [32] for a liquid film flowing over a uniformly heated slippery substrate. The critical Reynolds number corresponding to the H mode beyond which the flow becomes unstable was calculated analytically and expressed as a function of inclination angle, slip length, Marangoni number, and Biot number. They produced the result for the slip length under the frameworks of the Benney-type model and weighted residual three-equation model and compared the result with that of the linearized Navier-Stokes equations. It was displayed that the Benney-type model produces a good result only in the vicinity of the critical Reynolds number, whereas the weighted residual model produces a good result up to a moderate value of the Reynolds number. Their results also reestablished the fact that the phase speed of the traveling wave increases in the presence of wall slip as reported by Samanta *et al.* [32]. Ellaban *et al.* [34] explored the linear stability of a binary liquid film falling down a heated slippery inclined plane in the low Reynolds number regime. They reported the effects of Soret number, Marangoni number, and slip length on the hydrodynamic H mode and the thermocapillary S mode in the long-wave regime. From their results, it was evident that both slip length and the Marangoni number have a destabilizing effect on the H-mode and S-mode instabilities. Furthermore, they showed that the neutral curves corresponding to the H mode and S mode merge with each other with the increase in the values of the Marangoni number and slip length. Thiele *et al.* [35] and Sadiq *et al.* [36] investigated the instability of a gravity-driven flow over a heated porous substrate, while

Ogden *et al.* [37] investigated the instability of a gravity-driven flow over a wavy heated porous substrate. All these studies predicted the destabilizing effect of permeability on the H-mode instability. Bhat and Samanta [38] studied the effect of slip length on the instability of a surfactant-laden liquid film falling down an inclined plane for disturbances of arbitrary wavenumbers. A stabilizing influence of the slip length on the shear mode instability was demonstrated.

From the above literature survey, we have noticed that most of the studies regarding the liquid film flowing over a uniformly heated slippery substrate were two dimensional and confined in the low to moderate Reynolds number regime. As a result, the effect of spanwise wavenumber has not been examined on the most unstable modes, which generally has a stabilizing effect on the H mode that can be concluded from Squire’s theorem for the isothermal film flow. However, there was no analytical proof of Squire’s theorem for the nonisothermal flow configuration. This fact is also proved analytically and numerically in the present study for the nonisothermal flow configuration. Furthermore, previous studies paid attention to the hydrodynamic H mode and the thermocapillary S mode. There are not many investigations on the thermocapillary P mode and shear mode that have appeared in the finite wavenumber regime. In fact, investigation of the P mode is important because this mode is responsible for the steady convection rolls, where the fluid surface deformation does not play a significant role in this physical phenomenon [39]. On the other hand, the investigation of the shear mode is equally important because it appears in the high Reynolds number regime and sometimes dominates over the H mode depending on the value of the angle of inclination. In the present paper, we have accomplished a detailed parametric study on the individual modes (H mode, S mode, P mode, and shear mode) found analytically as well as numerically for a three-dimensional liquid film flowing over a uniformly heated slippery substrate. The long-wave approximation technique is used for solving the system of boundary value problems analytically. However, the Chebyshev spectral collocation method is used for solving the system of boundary value problems numerically for disturbances of arbitrary wavenumbers. We have recognized the hydrodynamic H mode and the thermocapillary S mode and P mode in the low to moderate Reynolds number regime, while the shear mode is found when the Reynolds number is large. The individual effect of Marangoni number, Biot number, Prandtl number, slip length, and spanwise wavenumber are deciphered on the different unstable temporal modes.

II. MATHEMATICAL FORMULATION

We consider a gravity-driven three-dimensional incompressible viscous liquid film flowing down a heated slippery inclined plane, where the inclined plane makes an angle θ with the horizontal as shown in Fig. 1. It is assumed that the inclined plane is uniformly heated with temperature $T = T_w$. As we are mainly interested in deciphering the thermocapillary instability at the surface of a three-dimensional falling liquid film, the physical properties of the liquid film, such as the density ρ and the dynamic viscosity μ , are assumed to be constants throughout the study; i.e., these physical properties

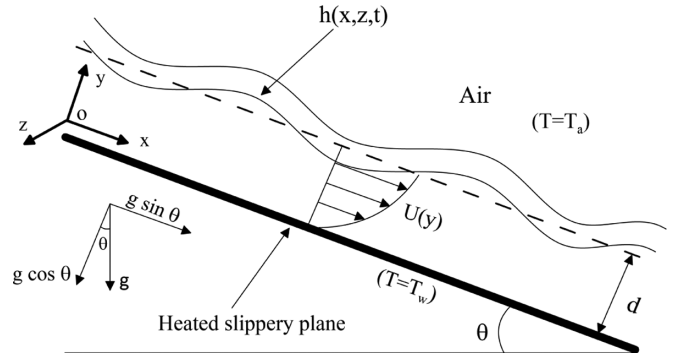


FIG. 1. Schematic diagram of a thin liquid film flowing down a heated slippery inclined plane.

of the liquid will not vary with the temperature. However, the surface tension σ will vary linearly with the temperature and can be determined by the following relation [40]:

$$\sigma(T) = \sigma_a - \gamma(T - T_a), \tag{1}$$

where T_a is the ambient temperature and σ_a is the surface tension at $T = T_a$. Here $\gamma = -\frac{d\sigma}{dT}|_{T=T_a} > 0$, as the surface tension of the liquid film decreases with the increasing value of the temperature. However, there are some special cases like water-alcohol solutions where the surface tension increases with the increasing value of the temperature [39]. The origin of the Cartesian coordinate system is taken on the slippery inclined plane and the axes x , y , and z are taken in streamwise, cross-stream, and spanwise directions, respectively. Here d is the thickness of the undisturbed liquid film, which is marked by a dashed line in Fig. 1, and $h(x, z, t)$ is the thickness of the disturbed liquid film. The governing equations for the nonisothermal liquid film flow, i.e., continuity, momentum, and energy equations, are as follows [39,41,42]:

$$\partial_x u + \partial_y v + \partial_z w = 0, \tag{2}$$

$$\rho(\partial_t u + u\partial_x u + v\partial_y u + w\partial_z u) = -\partial_x p + \mu(\partial_{xx} u + \partial_{yy} u + \partial_{zz} u) + \rho g \sin \theta, \tag{3}$$

$$\rho(\partial_t v + u\partial_x v + v\partial_y v + w\partial_z v) = -\partial_y p + \mu(\partial_{xx} v + \partial_{yy} v + \partial_{zz} v) - \rho g \cos \theta, \tag{4}$$

$$\rho(\partial_t w + u\partial_x w + v\partial_y w + w\partial_z w) = -\partial_z p + \mu(\partial_{xx} w + \partial_{yy} w + \partial_{zz} w), \tag{5}$$

$$\rho c_p(\partial_t T + u\partial_x T + v\partial_y T + w\partial_z T) = \kappa(\partial_{xx} T + \partial_{yy} T + \partial_{zz} T), \tag{6}$$

where u , v , w , p , and T are, respectively, the velocity components, pressure, and temperature of the liquid film. Here g is the gravitational acceleration, κ is the thermal conductivity, and c_p is the specific heat capacity at constant pressure. We assume that the thermal conductivity κ is not varying with the temperature. The above flow configuration is subjected to the following boundary conditions. At the inclined plane, $y = 0$, the streamwise and spanwise velocity components are nonzero because of the slippery plane. In this case,

the velocity components rather satisfy the Navier-slip and no-penetration boundary conditions while the temperature is uniform at the plane, and therefore, we can write [29,32,43–45]

$$u = \zeta_x \partial_y u, \quad v = 0, \quad w = \zeta_z \partial_y w, \quad T = T_w, \quad \text{at } y = 0, \tag{7}$$

where ζ_x and ζ_z are, respectively, the streamwise and spanwise dimensional slip lengths, and T_w is the temperature at the wall. In the current work, we restrict to the case of a slippery plane whose streamwise and spanwise slip lengths are equal,

i.e., $\zeta_x = \zeta_z = \zeta_w$. There is an experimental evidence that the value of slip length for the polydimethylsiloxane (PDMS) substrate is $\sim 250 \mu\text{m}$ [46], and therefore, its nondimensional value will be of order $\mathcal{O}(0.1)$ when the undisturbed liquid film thickness is about $d = 2.5 \text{ mm}$ [45,47]. At the liquid film surface, $y = h(x, z, t)$, the hydrodynamic stress is balanced by the surface stress induced by the surface tension times curvature of the liquid film surface and the Marangoni stress induced by the surface tension gradient due to the change of temperature. The dynamic boundary conditions corresponding to the above stress balance at $y = h(x, z, t)$ can be written as [39]

$$\begin{aligned} & \mu[(\partial_y u + \partial_x v)\{1 - (\partial_x h)^2\} + 2\partial_x h(\partial_y v - \partial_x u) - \partial_z h(\partial_z u + \partial_x w) - \partial_x h \partial_z h(\partial_z v + \partial_y w)] \\ & + \gamma[\partial_x T + \partial_x h \partial_y T] \sqrt{1 + (\partial_x h)^2 + (\partial_z h)^2} = 0, \end{aligned} \tag{8}$$

$$\begin{aligned} & \mu[(\partial_y w + \partial_z v)\{1 - (\partial_z h)^2\} + 2\partial_z h(\partial_y v - \partial_z w) - \partial_x h(\partial_z u + \partial_x w) - \partial_x h \partial_z h(\partial_y u + \partial_x v)] \\ & + \gamma[\partial_z T + \partial_z h \partial_y T] \sqrt{1 + (\partial_x h)^2 + (\partial_z h)^2} = 0, \end{aligned} \tag{9}$$

$$\begin{aligned} & -p[1 + (\partial_x h)^2 + (\partial_z h)^2] + 2\mu[\partial_x u(\partial_x h)^2 + \partial_z w(\partial_z h)^2 + \partial_x h \partial_z h(\partial_z u + \partial_x w) - \partial_x h(\partial_y u + \partial_x v) - \partial_z h(\partial_z v + \partial_y w) + \partial_y v] \\ & = \sigma[\partial_{xx} h\{1 + (\partial_z h)^2\} + \partial_{zz} h\{1 + (\partial_x h)^2\} - 2\partial_x h \partial_z h \partial_{xz} h]\{1 + (\partial_x h)^2 + (\partial_z h)^2\}^{-\frac{1}{2}}. \end{aligned} \tag{10}$$

Without loss of generality, the ambient pressure P_a is neglected from the normal stress boundary condition. Furthermore, to describe the heat transfer due to convection between air and liquid at the liquid film surface, $y = h(x, z, t)$, we use Newton’s law of cooling [24,39]:

$$\kappa \frac{(\partial_x T \partial_x h - \partial_y T + \partial_z T \partial_z h)}{\sqrt{1 + (\partial_x h)^2 + (\partial_z h)^2}} = \lambda(T - T_a), \tag{11}$$

where λ is the heat transfer coefficient. Finally, the evolution of the liquid film surface, $y = h(x, z, t)$, is described by the kinematic boundary condition

$$\partial_t h + u \partial_x h + w \partial_z h = v. \tag{12}$$

A. Dimensionless criterion

Now we introduce the following variables with star notation to nondimensionalize the governing equations and associated boundary conditions:

$$\begin{aligned} u^* &= \frac{u}{U_s}, \quad v^* = \frac{v}{U_s}, \quad w^* = \frac{w}{U_s}, \\ p^* &= \frac{pd}{2\mu U_s}, \quad x^* = \frac{x}{d}, \quad y^* = \frac{y}{d}, \\ z^* &= \frac{z}{d}, \quad h^* = \frac{h}{d}, \quad t^* = \frac{tU_s}{d}, \\ \sigma^* &= \frac{\sigma}{\sigma_a}, \quad T^* = \frac{T - T_a}{T_w - T_a}, \end{aligned} \tag{13}$$

where $\beta = \frac{\zeta_w}{d}$ is the nondimensional slip length and $U_s = \rho g d^2 \sin\theta(1 + 2\beta)/(2\mu)$ is the velocity at the liquid film surface for base flow with a constant thickness d . For our convenience, we have removed the star notation from the nondimensional variables in the subsequent formulation.

Using the above dimensionless criterion, the governing equations and the associated boundary conditions can be written as

$$\partial_x u + \partial_y v + \partial_z w = 0, \tag{14}$$

$$\begin{aligned} & \text{Re}(\partial_t u + u \partial_x u + v \partial_y u + w \partial_z u) \\ & = -2\partial_x p + (\partial_{xx} u + \partial_{yy} u + \partial_{zz} u) + \frac{2}{1 + 2\beta}, \end{aligned} \tag{15}$$

$$\begin{aligned} & \text{Re}(\partial_t v + u \partial_x v + v \partial_y v + w \partial_z v) \\ & = -2\partial_y p + (\partial_{xx} v + \partial_{yy} v + \partial_{zz} v) - \frac{2 \cot \theta}{1 + 2\beta}, \end{aligned} \tag{16}$$

$$\begin{aligned} & \text{Re}(\partial_t w + u \partial_x w + v \partial_y w + w \partial_z w) \\ & = -2\partial_z p + (\partial_{xx} w + \partial_{yy} w + \partial_{zz} w), \end{aligned} \tag{17}$$

$$\text{Pe}(\partial_t T + u \partial_x T + v \partial_y T + w \partial_z T) = (\partial_{xx} T + \partial_{yy} T + \partial_{zz} T), \tag{18}$$

$$u = \beta \partial_y u, \quad v = 0, \quad w = \beta \partial_y w, \quad T = 1, \quad \text{at } y = 0, \tag{19}$$

$$\begin{aligned} & (\partial_y u + \partial_x v)[1 - (\partial_x h)^2] + 2\partial_x h(\partial_y v - \partial_x u) - \partial_z h(\partial_z u + \partial_x w) \\ & - \partial_x h \partial_z h(\partial_z v + \partial_y w) \\ & = -2\text{Ma}[\partial_x T + \partial_x h \partial_y T] \sqrt{1 + (\partial_x h)^2 + (\partial_z h)^2}, \quad \text{at } y = h, \end{aligned} \tag{20}$$

$$\begin{aligned}
 &(\partial_y w + \partial_z v)[1 - (\partial_z h)^2] + 2\partial_z h(\partial_y v - \partial_z w) - \partial_x h(\partial_z u + \partial_x w) - \partial_x h \partial_z h(\partial_y u + \partial_x v) \\
 &= -2\text{Ma}[\partial_z T + \partial_z h \partial_y T] \sqrt{1 + (\partial_x h)^2 + (\partial_z h)^2}, \quad \text{at } y = h,
 \end{aligned} \tag{21}$$

$$\begin{aligned}
 &-p[1 + (\partial_x h)^2 + (\partial_z h)^2] + [\partial_x u(\partial_x h)^2 + \partial_z w(\partial_z h)^2 + \partial_x h \partial_z h(\partial_z u + \partial_x w) - \partial_x h(\partial_y u + \partial_x v) - \partial_z h(\partial_z v + \partial_y w) + \partial_y v] \\
 &= (\text{We} - \text{Ma } T)[\partial_{xx} h\{1 + (\partial_z h)^2\} + \partial_{zz} h\{1 + (\partial_x h)^2\}] - 2\partial_x h \partial_z h \partial_{xz} h\{1 + (\partial_x h)^2 + (\partial_z h)^2\}^{-\frac{1}{2}}, \quad \text{at } y = h,
 \end{aligned} \tag{22}$$

$$\frac{(\partial_x T \partial_x h - \partial_y T + \partial_z T \partial_z h)}{\sqrt{1 + (\partial_x h)^2 + (\partial_z h)^2}} = \text{Bi } T, \quad \text{at } y = h, \tag{23}$$

$$\partial_t h + u \partial_x h + w \partial_z h = v, \quad \text{at } y = h, \tag{24}$$

where $\text{Re} = \frac{\rho U_s d}{\mu}$ is the Reynolds number, which compares inertia to the viscous force, $\text{Ma} = \frac{\gamma(T_w - T_a)}{2\mu U_s}$ is the Marangoni number, which compares the Marangoni force to the viscous force, $\text{We} = \frac{\sigma_a}{2\mu U_s}$ is the Weber number, which compares the surface force due to the curvature of the liquid film surface to the viscous force, $\text{Bi} = \frac{\lambda d}{\kappa}$ is the Biot number, which compares the heat convection at the liquid film surface to the heat conduction within the liquid film, and $\text{Pe} = \rho c_p U_s d / \kappa = \text{RePr}$ is the Péclet number, where $\text{Pr} = \rho c_p \nu / \kappa$ is the Prandtl number. As we are interested in exploring the linear stability analysis of a three-dimensional nonisothermal base flow, we require the solution for the unidirectional parallel liquid film flow, the so-called the base flow with a constant liquid film thickness $y = 1$. The exact solution for the base flow equations can be expressed as

$$\bar{U}(y) = \frac{2y + 2\beta - y^2}{1 + 2\beta}, \quad \bar{V}(y) = 0, \tag{25}$$

$$\bar{W}(y) = 0, \quad 0 \leq y \leq 1, \tag{25}$$

$$\bar{P}(y) = \frac{1 - y}{1 + 2\beta} \cot \theta, \quad 0 \leq y \leq 1, \tag{26}$$

$$\bar{T}(y) = 1 - \left(\frac{\text{Bi}}{1 + \text{Bi}} \right) y, \quad 0 \leq y \leq 1. \tag{27}$$

Note that the base flow velocity is explicitly dependent on the slip length β , while the base flow temperature is dependent on the Biot number Bi . Furthermore, the base flow velocity is a parabolic function of y but the base flow temperature is a linear function of y .

B. Perturbation equations

To study the linear stability of the three-dimensional nonisothermal liquid film flowing down a slippery inclined plane, we impose an infinitesimal perturbation on the base flow. As a consequence, each flow variable of the disturbed flow can be decomposed as follows:

$$u = \bar{U} + u', \quad v = v', \quad w = w', \quad p = \bar{P} + p', \tag{28}$$

$$T = \bar{T} + T', \quad h = 1 + h',$$

where u' , v' , w' , p' , T' , and h' are the perturbation flow variables. Substituting the variable's decomposition (28) in

the nondimensional governing equations and boundary conditions (14)–(24) and linearizing with respect to the base flow solution, we get the following perturbation equations:

$$\partial_x u' + \partial_y v' + \partial_z w' = 0, \quad 0 \leq y \leq 1, \tag{29}$$

$$\begin{aligned}
 &\text{Re}(\partial_t u' + \bar{U} \partial_x u' + v' \partial_y \bar{U}) \\
 &= -2\partial_x p' + (\partial_{xx} u' + \partial_{yy} u' + \partial_{zz} u'), \quad 0 \leq y \leq 1,
 \end{aligned} \tag{30}$$

$$\begin{aligned}
 &\text{Re}(\partial_t v' + \bar{U} \partial_x v') = -2\partial_y p' + (\partial_{xx} v' \\
 &+ \partial_{yy} v' + \partial_{zz} v'), \quad 0 \leq y \leq 1,
 \end{aligned} \tag{31}$$

$$\begin{aligned}
 &\text{Re}(\partial_t w' + \bar{U} \partial_x w') = -2\partial_z p' + (\partial_{xx} w' + \partial_{yy} w' \\
 &+ \partial_{zz} w'), \quad 0 \leq y \leq 1,
 \end{aligned} \tag{32}$$

$$\begin{aligned}
 &\text{Pe}(\partial_t T' + \bar{U} \partial_x T' + v' \partial_y \bar{T}) \\
 &= (\partial_{xx} T' + \partial_{yy} T' + \partial_{zz} T'), \quad 0 \leq y \leq 1,
 \end{aligned} \tag{33}$$

$$\begin{aligned}
 &u' = \beta \partial_y u', \quad v' = 0, \quad w' = \beta \partial_y w', \\
 &T' = 0, \quad \text{at } y = 0,
 \end{aligned} \tag{34}$$

$$\begin{aligned}
 &\partial_y u' + \partial_x v' - [2/(1 + 2\beta)]h' \\
 &= -2\text{Ma} \left[\partial_x T' - \frac{\text{Bi}}{1 + \text{Bi}} \partial_x h' \right], \quad \text{at } y = 1,
 \end{aligned} \tag{35}$$

$$\begin{aligned}
 &\partial_y w' + \partial_z v' = -2\text{Ma} \left[\partial_z T' - \frac{\text{Bi}}{1 + \text{Bi}} \partial_z h' \right], \quad \text{at } y = 1, \\
 &\tag{36}
 \end{aligned}$$

$$\begin{aligned}
 &-p' + \frac{\cot \theta}{1 + 2\beta} h' + \partial_y v' \\
 &= \left(\text{We} - \frac{\text{Ma}}{1 + \text{Bi}} \right) (\partial_{xx} h' + \partial_{zz} h'), \quad \text{at } y = 1,
 \end{aligned} \tag{37}$$

$$\partial_y T' = \text{Bi} \left(\frac{\text{Bi}}{1 + \text{Bi}} h' - T' \right), \quad \text{at } y = 1, \tag{38}$$

$$\partial_t h' + \bar{U} \partial_x h' = v', \quad \text{at } y = 1. \tag{39}$$

C. Orr-Sommerfeld-type boundary value problem

Next we assume the solution of the perturbation equations (29)–(39) in the normal mode form

[48],

$$\left. \begin{aligned} u'(x, y, z, t) &= \hat{u}(y) \exp[i(k_x x + k_z z - \omega t)], \\ v'(x, y, z, t) &= \hat{v}(y) \exp[i(k_x x + k_z z - \omega t)], \\ w'(x, y, z, t) &= \hat{w}(y) \exp[i(k_x x + k_z z - \omega t)], \\ T'(x, y, z, t) &= \hat{\tau}(y) \exp[i(k_x x + k_z z - \omega t)], \\ p'(x, y, z, t) &= \hat{p}(y) \exp[i(k_x x + k_z z - \omega t)], \\ h'(x, z, t) &= \hat{\eta} \exp[i(k_x x + k_z z - \omega t)], \end{aligned} \right\} \quad (40)$$

where $\hat{u}(y)$, $\hat{v}(y)$, $\hat{w}(y)$, $\hat{\tau}(y)$, $\hat{p}(y)$, and $\hat{\eta}$ are the amplitudes of perturbation velocity components, perturbation temperature, perturbation pressure, and liquid film surface deformation, respectively. Here k_x and k_z are, respectively, the streamwise and spanwise wavenumbers, $\omega = k_x c$ is the angular frequency, c is the wave speed, and $k = \sqrt{k_x^2 + k_z^2}$ is the total wavenumber of the infinitesimal disturbance. Inserting the normal mode solution (40) in the perturbation equations (29)–(39) and eliminating the pressure terms, we get the following coupled system of boundary value problems for the perturbation normal velocity and perturbation temperature, respectively:

$$(D^2 - k^2)^2 \hat{v} = i\text{Re} \left[(k_x \bar{U} - \omega)(D^2 - k^2) + \frac{2k_x}{1 + 2\beta} \right] \hat{v}, \quad 0 \leq y \leq 1, \quad (41)$$

$$(D^2 - k^2) \hat{\tau} = \text{Pe} \left[i(k_x \bar{U} - \omega) \hat{\tau} - \left(\frac{\text{Bi}}{1 + \text{Bi}} \right) \hat{v} \right], \quad 0 \leq y \leq 1, \quad (42)$$

$$\hat{v} = 0, \quad \hat{\tau} = 0, \quad D\hat{v} - \beta D^2 \hat{v} = 0, \quad \text{at } y = 0, \quad (43)$$

$$(D^2 + k^2) \hat{v} + 2k^2 \text{Ma} \left[\hat{\tau} - \frac{\text{Bi}}{1 + \text{Bi}} \hat{\eta} \right] + \frac{2ik_x}{1 + 2\beta} \hat{\eta} = 0, \quad \text{at } y = 1, \quad (44)$$

$$[D^2 - 3k^2 + i\text{Re}(\omega - k_x)] D\hat{v} - 2k^2 \hat{\eta} \times \left[k^2 \left(\text{We} - \frac{\text{Ma}}{1 + \text{Bi}} \right) + \frac{\cot \theta}{1 + 2\beta} \right] = 0, \quad \text{at } y = 1, \quad (45)$$

$$D\hat{\tau} + \text{Bi} \left[\hat{\tau} - \frac{\text{Bi}}{1 + \text{Bi}} \hat{\eta} \right] = 0, \quad \text{at } y = 1, \quad (46)$$

$$\hat{v} + i(\omega - k_x) \hat{\eta} = 0, \quad \text{at } y = 1, \quad (47)$$

where $D = \frac{d}{dy}$ is the differential operator. In the present study, we have investigated the temporal stability analysis, and thereby, the wavenumber k will be considered as a real number, while the wave speed c or, equivalently, the angular frequency ω will be considered as a complex number.

III. ANALYTICAL SOLUTION OF THE BOUNDARY VALUE PROBLEM

A. Streamwise perturbation in the long-wave regime

In order to perform the temporal stability analysis, we use the long-wave asymptotic approach as proposed by Yih [10]. From Squire's theorem [48,49], we know that the two-

dimensional disturbance begins to become unstable at a lower Reynolds number than that of the three-dimensional disturbance. For this reason, the long-wave analysis will be carried out for the two-dimensional disturbances with streamwise wavenumber. The analytical derivation of Squire's theorem for the nonisothermal flow configuration is performed in Appendix A. Consequently, we choose $k_z = 0$ and $k_x = k$. Furthermore, due to the consideration of two-dimensional flow configuration, the perturbation velocity components can be expressed in terms of the perturbation stream function $\psi'(x, y, t)$ as

$$u'(x, y, t) = \partial_y \psi', \quad v'(x, y, t) = -\partial_x \psi', \quad (48)$$

where the perturbation stream function is expressed in the normal mode form

$$\psi'(x, y, t) = \hat{\phi}(y) \exp[ik(x - ct)], \quad (49)$$

where $\hat{\phi}(y)$ is the amplitude of the stream function. Using Eq. (49), we can write $\hat{v}(y) = -ik\hat{\phi}(y)$, which is further substituted in the coupled system of boundary value problems (41)–(47) for the long-wave stability analysis [24]. Next the variables $\hat{\phi}$, $\hat{\tau}$, $\hat{\eta}$, and c are represented as the sum of infinite series in the limit $k \rightarrow 0$ as follows:

$$\left. \begin{aligned} \hat{\phi}(y) &= \sum_{n=0}^{\infty} \phi_n k^n, \quad \hat{\tau}(y) = \sum_{n=0}^{\infty} \tau_n k^n, \\ \hat{\eta} &= \sum_{n=0}^{\infty} \eta_n k^n, \quad c = \sum_{n=0}^{\infty} c_n k^n, \end{aligned} \right\} \quad (50)$$

where n belongs to the set of non-negative integers.

B. Zero-order approximation

Substituting Eq. (50) into the boundary value problems (41)–(47) and collecting the leading order [$\mathcal{O}(k^0)$] equations, we get

$$D^4 \phi_0(y) = 0, \quad D^2 \tau_0(y) = 0, \quad 0 \leq y \leq 1, \quad (51)$$

$$\phi_0(y) = 0, \quad \tau_0(y) = 0,$$

$$D\phi_0(y) - \beta D^2 \phi_0(y) = 0, \quad \text{at } y = 0, \quad (52)$$

$$D^2 \phi_0(y) - \frac{2}{1 + 2\beta} \eta_0 = 0, \quad D^3 \phi_0(y) = 0, \quad \text{at } y = 1, \quad (53)$$

$$D\tau_0(y) + \text{Bi} \tau_0(y) - \frac{\text{Bi}^2}{1 + \text{Bi}} \eta_0 = 0, \quad \text{at } y = 1, \quad (54)$$

$$\phi_0(y) - (c_0 - 1)\eta_0 = 0, \quad \text{at } y = 1. \quad (55)$$

The solution of the zero-order equations (51)–(55) is given by

$$\phi_0(y) = \frac{(y^2 + 2\beta y)\eta_0}{1 + 2\beta}, \quad \tau_0(y) = \frac{\text{Bi}^2 y \eta_0}{(1 + \text{Bi})^2}. \quad (56)$$

It can be clearly observed that the zero-order solution $\phi_0(y)$ depends on the slip length β , while $\tau_0(y)$ depends on the Biot number Bi. However, the zero-order solution is independent of the Marangoni number Ma and the Péclet number Pe. Now with the help of the zero-order kinematic boundary condition (55), one can obtain the zero-order phase speed c_0 for the infinitesimal disturbance,

$$c_0 = 2. \quad (57)$$

Note that the zero-order phase speed is real and equal to two times the surface velocity of base flow. In particular, this phase speed is associated with the surface mode or H mode, which generally appears due to the infinitesimal perturbation of the liquid film surface [50].

C. First-order approximation

Now we collect the first-order [$\mathcal{O}(k)$] equations:

$$D^4 \phi_1(y) + i\text{Re}\{\phi_0(y)D^2 \bar{U}(y) + \{c_0 - \bar{U}(y)\}D^2 \phi_0(y)\} = 0, \quad 0 \leq y \leq 1, \quad (58)$$

$$D^2 \tau_1(y) + i\text{Pe}\{c_0 - \bar{U}(y)\}\tau_0(y) - \frac{i\text{PeBi}}{1 + \text{Bi}}\phi_0(y) = 0, \quad 0 \leq y \leq 1, \quad (59)$$

$$\phi_1(y) = 0, \quad \tau_1(y) = 0, \quad D\phi_1(y) - \beta D^2 \phi_1(y) = 0, \quad \text{at } y = 0, \quad (60)$$

$$D^2 \phi_1(y) + 2i\text{Ma}\left[\tau_0(y) - \frac{\text{Bi}}{1 + \text{Bi}}\eta_0\right] - \frac{2\eta_1}{1 + 2\beta} = 0, \quad \text{at } y = 1, \quad (61)$$

$$D^3 \phi_1(y) + i\text{Re}(c_0 - 1)D\phi_0(y) - \frac{2i\eta_0 \cot \theta}{1 + 2\beta} = 0, \quad \text{at } y = 1, \quad (62)$$

$$D\tau_1(y) + \text{Bi}\left[\tau_1(y) - \frac{\text{Bi}}{1 + \text{Bi}}\eta_1\right] = 0, \quad \text{at } y = 1, \quad (63)$$

$$\phi_1(y) + (1 - c_0)\eta_1 - c_1\eta_0 = 0, \quad \text{at } y = 1. \quad (64)$$

Here the Weber number We is considered of order $\mathcal{O}(1)$, and thereby it does not appear in the first-order normal stress boundary condition (62). Now solving the first-order equations (58)–(64), we get the expressions of $\phi_1(y)$ and $\tau_1(y)$, which are given in Appendix B. Putting the expressions of $\phi_1(y)$ and $\tau_1(y)$ in the first-order kinematic boundary condition (64), we get the expression of c_1 ,

$$c_1 = i(a_0 + a_1\text{Re} + a_2 \cot \theta), \quad (65)$$

where

$$a_0 = \frac{(1 + 2\beta)\text{Ma Bi}}{(1 + \text{Bi})^2},$$

$$a_1 = \frac{(1 + \beta)\{2 + 5\beta(2 + 3\beta)\}}{15(1 + 2\beta)^2},$$

$$a_2 = -\frac{2(1 + 3\beta)}{3 + 6\beta}.$$

Note that the expression of c_1 is purely imaginary. Furthermore, the effects of the Marangoni number Ma and the Biot number Bi are introduced in the expression of c_1 . With the aid of the neutral stability condition ($c_i \approx kc_1 = 0$) in the limit $k \rightarrow 0$, the critical value of the Reynolds number, Re_c , for the surface mode or H mode is calculated and can be written as

$$\text{Re}_c = \frac{10(1 + 2\beta)(1 + 3\beta) \cot \theta - 15(1 + 2\beta)^3\{\text{Ma Bi}/(1 + \text{Bi})^2\}}{4(1 + \beta)\{2 + 5\beta(2 + 3\beta)\}}. \quad (66)$$

It can be clearly observed that the expression of the critical Reynolds number coincides with that of Samanta *et al.* [32] and Bhat and Samanta [38] in the case of an isothermal film flowing down a slippery inclined plane ($\text{Ma} \rightarrow 0, \text{Bi} \rightarrow 0$). Furthermore, the critical Reynolds number recovers the result of Trevelyan and Kalliadasis [51] if the slip length β is set to zero. In addition, the present critical Reynolds number for the H mode coincides with that of Sadiq *et al.* [36], if we consider the average velocity of a unidirectional parallel flow over a nonslippery plane as the characteristic velocity scale preferred by them. Figure 2(a) demonstrates the variation of the critical Reynolds number with the Marangoni number when the slip length β varies. It should be noted that the critical Reynolds number reduces with the increasing values of the Marangoni number and the slip length. Hence, one can expect the destabilizing influences of the Marangoni number and the slip length on the surface mode or H mode. In particular, the surface instability induced by the H mode initiates due to the external perturbation just after the flow Reynolds number exceeds the critical value Re_c . As discussed by Kalliadasis *et al.* [39], the temperature is a maximum at the crest while it is a minimum at the trough due to the difference in height of a perturbed liquid film surface [see also Eq. (56)]. This fact causes a minimum surface tension at the crest and a maximum surface tension

at the trough of the perturbed film surface. If the Marangoni number is increased, the temperature difference between the liquid and the ambient gas phase is enhanced, which reduces the surface tension of the liquid and yields a destabilizing effect to the surface mode or H mode. On the other hand, the base flow rate increases with the rising values of the slip length and renders a destabilizing effect to the surface mode or H mode.

D. Second-order approximation

Now we consider the second-order [$\mathcal{O}(k^2)$] equations:

$$D^4 \phi_2(y) + i\text{Re}(c_0 - \bar{U})D^2 \phi_1(y) + (i\text{Re } c_1 - 2)D^2 \phi_0(y) + i\text{Re}\phi_1(y)D^2 \bar{U}(y) = 0, \quad 0 \leq y \leq 1, \quad (67)$$

$$D^2 \tau_2(y) + i\text{Pe}\{c_0 - \bar{U}(y)\}\tau_1(y) + (i\text{Pe } c_1 - 1)\tau_0(y) - \frac{i\text{PeBi}}{1 + \text{Bi}}\phi_1(y) = 0, \quad 0 \leq y \leq 1, \quad (68)$$

$$\phi_2(y) = 0, \quad \tau_2(y) = 0, \quad D\phi_2(y) - \beta D^2 \phi_2(y) = 0, \quad \text{at } y = 0, \quad (69)$$

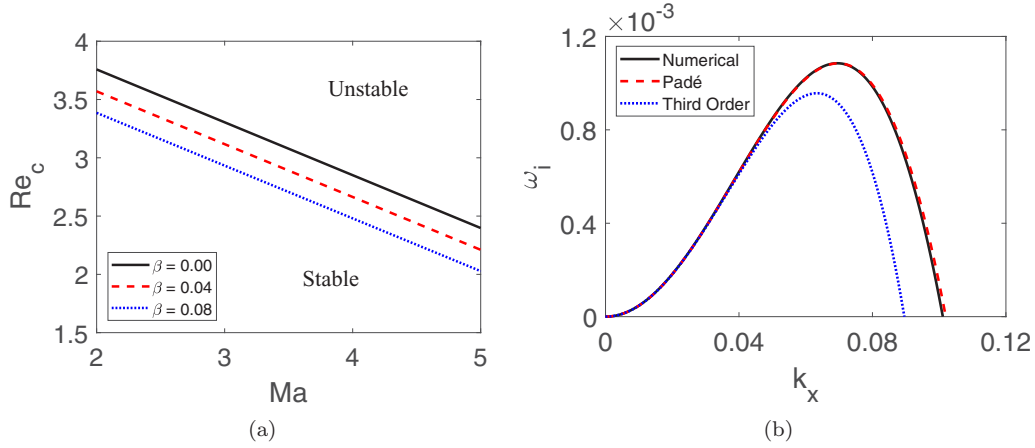


FIG. 2. (a) Variation of the critical Reynolds number Re_c with the Marangoni number Ma for the surface mode or H mode when the slip length β varies. Solid, dashed, and dotted lines represent the results for $\beta = 0$, $\beta = 0.04$, and $\beta = 0.08$, respectively. The other parameter values are $Bi = 1.44$ and $\theta = 15^\circ$. (b) Comparison of temporal growth rate for the H mode with the results obtained from the Padé approximation and numerical solution. Solid, dashed, and dotted lines represent the results of numerical solution, Padé approximation, and third-order long-wave analytical solution, respectively. The other parameter values are $Re = 5$, $Ka = 250$, $Pr = 7$, $Bi = 1$, $Ma = 5$, and $\theta = 15^\circ$.

$$D^2\phi_2(y) + \phi_0(y) + 2iMa\tau_1(y) - \frac{2iMaBi\eta_1}{1+Bi} - \frac{2\eta_2}{1+2\beta} = 0, \quad \text{at } y = 1, \quad (70)$$

$$D^3\phi_2(y) + iRe(c_0 - 1)D\phi_1(y) + (iRe c_1 - 3)D\phi_0(y) - \frac{2i\eta_1 \cot \theta}{1+2\beta} = 0, \quad \text{at } y = 1, \quad (71)$$

$$D\tau_2(y) + Bi \left[\tau_2(y) - \frac{Bi\eta_2}{1+Bi} \right] = 0, \quad \text{at } y = 1, \quad (72)$$

$$\phi_2(y) + (1 - c_0)\eta_2 - c_1\eta_1 - c_0\eta_2 = 0, \quad \text{at } y = 1. \quad (73)$$

Solving the second-order equations (67)–(73), we get the expression of c_2 for the surface mode or H mode:

$$c_2 = \frac{b_0 + b_1Bi + b_2Bi^2 + b_0Bi^3}{60(1+Bi)^3} + b_3ReMaBi + b_4Re \cot \theta + b_5Re^2, \quad (74)$$

where

$$\begin{aligned} b_0 &= -120(1+2\beta), \\ b_1 &= -5[72(1+2\beta) + MaPe(3+8\beta)], \\ b_2 &= 7MaPe - 360(1+2\beta), \\ b_3 &= \frac{19+2\beta[57+40\beta(3+2\beta)]}{20(1+Bi)^2(1+2\beta)}, \\ b_4 &= \frac{8[5+7\beta\{5+3\beta(4+3\beta)\}]}{63(1+2\beta)^2}, \\ b_5 &= \frac{160(1+\beta)}{315(1+2\beta)^3} \\ &\quad + \frac{16\beta(1+\beta)[90+7\beta\{46+15\beta(5+3\beta)\}]}{315(1+2\beta)^3}. \end{aligned}$$

Obviously, c_2 is real. Similarly, solving the third-order $[\mathcal{O}(k^3)]$ equations, we obtain the expression of c_3 for the surface mode or H mode,

$$c_3 = -i \left[\frac{(h_0 + h_1Ma + h_2Ma^2)}{50400(1+Bi)^5(1+2\beta)} - \frac{(h_3 + h_4Ma + h_5Ma^2)Re}{25200(1+Bi)^4(1+2\beta)^2} + \frac{h_6Re^2}{4989600(1+Bi)^2(1+2\beta)^3} + \frac{h_7Re^3}{2027025(1+2\beta)^4} \right], \quad (75)$$

where the coefficients h_i ($i = 0, \dots, 7$) are given in Appendix C. Note that c_3 is purely imaginary. Hence, the complex wave speed c for the surface mode or H mode can be written as

$$c = c_0 + kc_1 + k^2c_2 + k^3c_3 + \mathcal{O}(k^4) = c_r + ic_i. \quad (76)$$

If $c_i > 0$, the infinitesimal disturbance induced by the surface mode or H mode will grow exponentially with time and the disturbance will be unstable. Figure 2(b) shows the comparison of temporal growth rate for the H mode with the

results obtained from the Padé approximation and numerical solution. The discussion of the Padé approximation is supplied in Appendix D, while the numerical technique for solving the boundary value problems is discussed in Sec. IV. Note that the Padé approximation almost captures the result of numerical solution. However, the long-wave third-order result deviates from the numerical solution except in the vicinity of $k_x = 0$, because the long-wave approximation is valid in the limit $k_x \rightarrow 0$. The above result indicates that the Padé approximation is more accurate than the higher-order long-wave expansion.

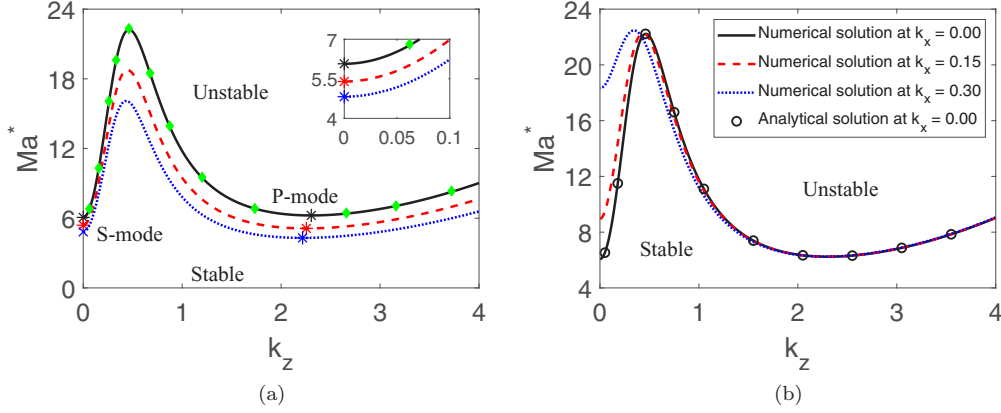


FIG. 3. Neutral stability curve for the stationary instability in the (k_z, Ma^*) plane when $k_x = 0$. Solid, dashed, and dotted lines represent the results for $\beta = 0, \beta = 0.04$, and $\beta = 0.08$, respectively. The other parameter values are $Re_k = 1, We_k = 120, Pe_k = Pr_k = 7, Bi = 1.44$, and $\theta = 15^\circ$. The diamond points are the results of Kalliadasis *et al.* [39]. The star points represent the onset of instabilities for the S mode and P mode. (b) Neutral stability curve for the stationary instability in the (k_z, Ma^*) plane for different values of k_x and $\beta = 0$. Solid, dashed, and dotted lines represent the numerical results for $k_x = 0, k_x = 0.15$, and $k_x = 0.30$, respectively. The circular points represent the analytical result when $k_x = 0$.

E. Spanwise perturbation in the arbitrary wavenumber regime

Following the study of Kalliadasis *et al.* [39], the boundary value problems (41)–(47) will be further studied for the two-dimensional disturbances with spanwise wavenumber. Consequently, we choose $k_x = 0$ and $k_z = k$. As a result, the boundary value problems (41)–(47) will be simplified into the following form:

$$(D^2 - k^2)^2 \hat{v} + iRe \omega (D^2 - k^2) \hat{v} = 0, \quad 0 \leq y \leq 1, \quad (77)$$

$$(D^2 - k^2) \hat{t} + Pe \left[i\omega \hat{t} + \left(\frac{Bi}{1 + Bi} \right) \hat{v} \right] = 0, \quad 0 \leq y \leq 1, \quad (78)$$

$$\hat{v} = 0, \quad \hat{t} = 0, \quad D\hat{v} - \beta D^2 \hat{v} = 0, \quad \text{at } y = 0, \quad (79)$$

$$(D^2 + k^2) \hat{v} + 2k^2 Ma \left[\hat{t} - \frac{Bi}{1 + Bi} \hat{\eta} \right] = 0, \quad \text{at } y = 1, \quad (80)$$

$$\begin{aligned} [D^2 - 3k^2 + iRe\omega]D\hat{v} - 2k^2 \hat{\eta} \left[k^2 \left(We - \frac{Ma}{1 + Bi} \right) \right. \\ \left. + \frac{\cot \theta}{1 + 2\beta} \right] = 0, \quad \text{at } y = 1, \end{aligned} \quad (81)$$

$$D\hat{t} + Bi \left[\hat{t} - \frac{Bi}{1 + Bi} \hat{\eta} \right] = 0, \quad \text{at } y = 1, \quad (82)$$

$$\hat{v} + i\omega \hat{\eta} = 0, \quad \text{at } y = 1. \quad (83)$$

Here we are mainly interested in exploring the stationary instability in the arbitrary wavenumber regime, and thereby, we use the condition $\omega_r = 0$. Furthermore, for computing the neutral stability curve we set $\omega_i = 0$. Using the above criteria, one can obtain the neutral stability condition for the stationary instability,

$$Ma^* = \frac{4k(k \cosh k + Bi \sinh k) \{2k - \sinh 2k + 2k\beta(1 - \cosh 2k)\}}{2Pe[k^3(1 + 4\beta) \cosh k - \sinh^3 k + k\beta\{(\cosh k - 2 \cosh 3k - 8k \sinh k)/2\}] - \frac{8k^5(1+2\beta) \cosh k}{\cot \theta / (1+2\beta) + k^2(We - Ma^*/Bi)}}, \quad (84)$$

where $Ma^* = Ma Bi / (1 + Bi)$. Note that the above expression (84) coincides with that of the liquid film flowing down a uniformly heated inclined plane [39] if the slip length β is set to zero. A little difference found in coefficients is the consequence of the choice of various nondimensional scales. Furthermore, the above expression (84) recovers the result of Pearson [52] for a horizontal liquid film over a uniformly heated plane with a nondeformable film surface in the limits $\cot \theta \rightarrow \infty$ and $We \rightarrow \infty$. In accordance with the study of Kalliadasis *et al.* [39], the neutral stability curve for the stationary instability is plotted in the (k_z, Ma^*) plane when the slip length β varies. The result can be found in Fig. 3(a) when $Re_k = 1, Pe_k = Pr_k = 7, Bi = 1.44$, and $\theta = 15^\circ$ are fixed. In order to recreate the result of Kalliadasis *et al.* [39],

we have considered the relations $We = We_k / (1 + 2\beta)$ and $Pe = (3/2)(1 + 2\beta)Pe_k$, where We_k and Pe_k are the parameter values of Kalliadasis *et al.* [39]. It is evident that there exist two local minima for each neutral stability curve. In fact, the local minimum appearing at $k = 0$ is associated with the threshold of instability for the long-wave S mode, while the local minimum appearing in the finite spanwise wavenumber regime is associated with the threshold of instability for the short-wave P mode [18]. In particular, the S mode and P mode emerge due to the infinitesimal perturbation of the temperature at the liquid film surface. For this reason, these modes are also referred to as the thermocapillary modes. Hence in the finite wavenumber regime, the thermocapillary instability is dominated by the P mode rather than the S mode. As

discussed by Kalliadasis *et al.* [39], the S mode plays a role in the long-wave film surface deformation, while the P mode is responsible for the steady convection rolls. The important result is that the threshold of instabilities for the S mode and P mode depletes with the increasing value of β , and ensures the destabilizing effect of β on the S mode and P mode. Furthermore, the current result accurately recreates the result of Kalliadasis *et al.* [39] in the limit $\beta \rightarrow 0$. In order to see the effect of streamwise wavenumber on the S mode and P mode, the neutral curve is also plotted for nonzero values of the streamwise wavenumber k_x . This result is computed numerically and shown in Fig. 3(b). Note that the onset of instability for the thermocapillary S mode moves up as long as the streamwise wavenumber k_x increases, which ensures the destabilizing influence of the streamwise wavenumber on the thermocapillary S mode. Furthermore, the neutral curve obtained numerically coincides with that obtained analytically when $k_x = 0$.

IV. NUMERICAL SOLUTION OF THE BOUNDARY VALUE PROBLEM

Now the linear stability of the given flow configuration will be explored for disturbances of arbitrary wavenumbers. To do that, the boundary value problems (41)–(47) will be solved numerically by using the Chebyshev spectral collocation method proposed by Schmid and Henningson [53]. To this end, the boundary value problems (41)–(47) are converted into a generalized matrix eigenvalue problem as follows:

$$\mathcal{A}\xi = \omega\mathcal{B}\xi, \quad (85)$$

where ω is the eigenvalue and $\xi = [\hat{v}, \hat{t}]^T$ is the associated eigenvector. The matrices \mathcal{A} and \mathcal{B} can be expressed as follows:

$$\mathcal{A} = \begin{pmatrix} \mathcal{A}_{11} & 0 \\ \mathcal{A}_{21} & \mathcal{A}_{22} \end{pmatrix} \quad \text{and} \quad \mathcal{B} = \begin{pmatrix} \mathcal{B}_{11} & 0 \\ 0 & \mathcal{B}_{22} \end{pmatrix}, \quad (86)$$

where

$$\begin{aligned} \mathcal{A}_{11} &= i\text{Re}k_x \left[\bar{U}(D^2 - k^2) + \frac{2}{1 + 2\beta} \right] - (D^2 - k^2)^2, \\ \mathcal{A}_{21} &= -\frac{\text{Pe Bi}}{1 + \text{Bi}}, \quad \mathcal{A}_{22} = i\text{Pe}k_x \bar{U} - (D^2 - k^2), \\ \mathcal{B}_{11} &= i\text{Re}(D^2 - k^2), \quad \mathcal{B}_{22} = i\text{Pe}, \quad D = \frac{d}{dy}. \end{aligned}$$

The eigenvalue problem (85) is closed by applying the boundary conditions (43)–(47). In fact, in the Chebyshev spectral collocation method, the amplitude function $\xi(y)$ is expanded in a truncated series of the Chebyshev polynomials [48],

$$\xi(y) = \sum_{i=0}^N \xi_i T_i(y), \quad (87)$$

where N is the number of Chebyshev polynomials and ξ_i 's are unknown Chebyshev coefficients to be determined from the numerical simulation. As the Chebyshev polynomials $T_i(y)$ are defined over the domain $[-1, 1]$, the liquid layer domain $[0, 1]$ is shifted to $[-1, 1]$ by applying a transformation

$y = (x + 1)/2$. As a result, the derivatives are replaced by $D \rightarrow 2D$, $D^2 \rightarrow 4D^2$, \dots . Inserting Eq. (87) into the matrix eigenvalue problem (85), the Chebyshev functions are evaluated at the Gauss-Lobatto collocation points $x_j = \cos(\pi j/N)$, which are extrema of the Chebyshev polynomials, where $j = 0, \dots, N$.

A. Validation of the numerical code

First of all, the present numerical code is verified by comparing the numerical results with the available results existing in the literature. Following Ding *et al.* [33], the numerical results are reproduced for the temporal growth rate ω_i with the streamwise wavenumber $k_x = k$ induced by the surface mode or H mode when $\text{Re} = 15.75$, $\text{Ka} = 9655$, $\theta = \pi/2$, $\text{Pr} = 0.01$, $B = 0.32$, $\beta = 0.025$, and $k_z = 0$. Figure 4(a) displays the temporal growth rate for three different values of M , or equivalently, the Marangoni number Ma . In order to reproduce the results of Ding *et al.* [33], we have rescaled the nondimensional parameters using the following relations: $M = \text{Ma}(2\text{Re})^{2/3}(1 + 2\beta)^{1/3}$, $B = \text{Bi}(1 + 2\beta)^{1/3}/(2\text{Re})^{1/3}$, and $\text{Ka} = \text{We}(2\text{Re})^{2/3}(1 + 2\beta)^{1/3}$, where Ka is the Kapitza number which depends only on the physical properties of the liquid. Note that the current numerical results are found to be in good agreement with the numerical results of Ding *et al.* [33]. Obviously, the temporal growth rate ω_i induced by the surface mode or H mode intensifies with the increasing value of the Marangoni number as expected, because the Marangoni number has a destabilizing effect on the surface mode [see also Fig. 2(a)]. On the other hand, Fig. 4(b) displays the neutral stability curve in the (Re, k_x) plane for different values of M when $\text{Ka} = 250$, $\theta = 15^\circ$, $\text{Pr} = 7$, $B = 1$, $\beta = 0$, and $k_z = 0$. In this case, the results are reproduced for the surface mode or H mode and the thermocapillary S mode and compared with that of Kalliadasis *et al.* [39]. Again we have seen an excellent agreement between them. In particular, we have found only one neutral stability curve generated by the H mode in the (Re, k_x) plane when $M = 0$, as expected. As soon as $M \neq 0$, two neutral stability curves emerge. One associated with the S mode appears in the low Reynolds number regime, while the other one associated with the H mode appears when the Reynolds number exceeds its critical value given in Eq. (66). Obviously, the onset of instability induced by the H mode and the onset of stability for the S mode remain on the Re axis ($k_x = 0$) when $M = 15$. In particular, the H-mode instability emerges in the long-wave regime due to the perturbation of the film surface when the Reynolds number exceeds its threshold value. However, the S-mode instability generated by the Marangoni stress emerges in the long-wave regime due to the infinitesimal temperature perturbation at the film surface when the Reynolds number is very low ($\text{Re} \rightarrow 0$). As soon as the Reynolds number increases, the inertia force intensifies and gradually dominates over the Marangoni force. As a result, the S-mode instability weakens, and eventually dies down with increasing Re. Obviously, there exists a range of the Reynolds number where the S-mode instability is fully damped when $M = 15$. Apparently, it seems that the inertia force has a stabilizing effect on the thermocapillary S mode. If the Reynolds number is further increased, the H-mode

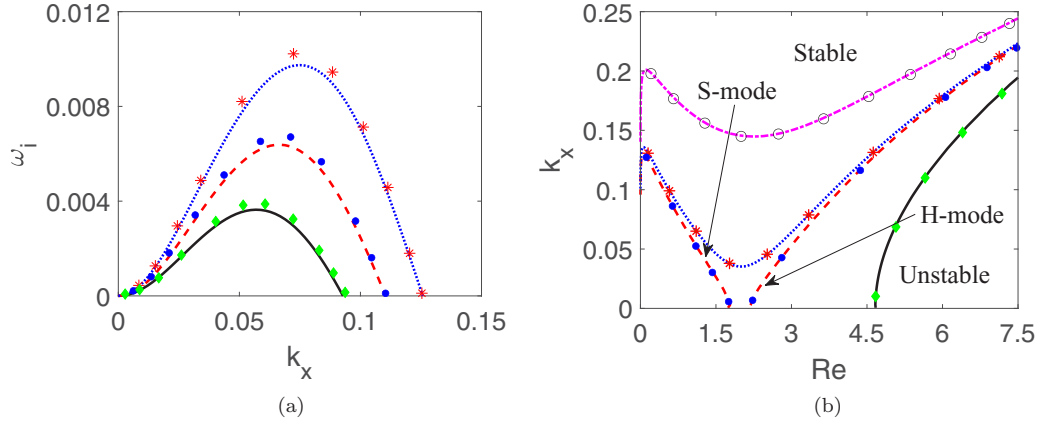


FIG. 4. (a) Variation of the temporal growth rate ω_i for the surface mode or H mode with streamwise wavenumber k_x for different values of M when $\text{Re} = 15.75$, $\text{Ka} = 9655$, $\theta = \pi/2$, $\text{Pr} = 0.01$, $B = 0.32$, $\beta = 0.025$, and $k_z = 0$. Solid, dashed, and dotted lines stand for $M = -96.55$, $M = 0$, and $M = 96.55$, respectively. The symbolic points are the results of Ding *et al.* [33]. (b) Variation of the neutral stability curves in the (Re, k_x) plane for different values of M when $\text{Ka} = 250$, $\theta = 15^\circ$, $\text{Pr} = 7$, $B = 1$, $\beta = 0$, and $k_z = 0$. Solid, dashed, dotted, and dash-dotted lines stand for $M = 0$, $M = 15$, $M = 16$, and $M = 30$, respectively. The symbolic points are the results of Kalliadasis *et al.* [39].

instability emerges when the Reynolds number exceeds the critical Reynolds number. Indeed, we have found a range of the Reynolds number where both H mode and S mode are stable to infinitesimal disturbances when $M = 15$. On the other hand, these two neutral stability curves merge with each other with the increasing value of M ($M = 16$) and generate a single onset of stability. Note that the onset of stability shifts in the finite streamwise wavenumber regime with increasing M when $k_z = 0$. This fact indicates the destabilizing influence of M . In addition, for further verification with the analytical result, we have calculated the critical Reynolds number numerically for the surface mode or H mode and compared with that of the analytical result in Table I when the parameter M varies. It can be clearly observed that the analytical and numerical results are in good agreement when $\text{Ka} = 250$, $\theta = 15^\circ$, $\text{Pr} = 7$, $B = 1$, and $\beta = 0$. Furthermore, the critical Reynolds number for the H mode decreases with the increasing value of M , which is fully consistent with the result shown in Fig. 2(a).

B. Effect of the Marangoni number

In this section, we discuss the individual effect of M or, equivalently, the Marangoni number Ma on the different un-

TABLE I. Comparison between the analytical and numerical values of the critical Reynolds number Re_c for the surface mode or H mode when the parameter M varies. The other parameter values are $\text{Ka} = 250$, $\theta = 15^\circ$, $\text{Pr} = 7$, $B = 1$, and $\beta = 0$.

M	Analytical value (Re_c)	Numerical value (Re_c)
5	4.1600	4.1633
7	3.9264	3.9296
9	3.6594	3.6541
11	3.3521	3.3545
13	2.9522	2.9481
15	2.1596	2.1527

stable modes. Numerically, we have found the existence of three distinct modes, the so-called H mode, S mode, and P mode, for low to moderate values of the Reynolds number. However, the shear mode emerges when the Reynolds number is very large [12–14,54]. These distinct modes are demonstrated in Fig. 5 for the different sets of parameter values. In fact, these distinct modes are recognized by their phase speeds which are completely different for H mode, S mode, P mode, and shear mode. In Fig. 6(a), the neutral stability curve for the H mode is plotted in the (Re, k_x) plane for different values of M or, equivalently, the different values of the Marangoni number when $\text{Ka} = 250$, $\theta = 15^\circ$, $\text{Pr} = 7$, $B = 1$, $\beta = 0.02$, and $k_z = 0$. It is observed that in the vicinity of the threshold of instability, the unstable region induced by the H mode enhances with the increase in the value of M . Consequently, the critical Reynolds number Re_c reduces, and just after that the H-mode instability initiates. This fact clearly indicates that the Marangoni number or, equivalently, the parameter M has a destabilizing effect on the H mode, which was previously reported by Hu *et al.* [23], Ding *et al.* [33], and Ellaban *et al.* [34] for a falling film over a uniformly heated plane. However, the unstable region for the H mode slightly reduces in the moderate Reynolds number regime with the increase in the value of M . This result is fully opposite to the effect of M on the H-mode instability in the region close to the threshold of instability. In order to confirm these long-wave destabilizing and short-wave stabilizing influences of M on the H mode, the temporal growth rate is plotted in Fig. 6(b) for two different values of the Reynolds number selected from the destabilizing and stabilizing zones shown in Fig. 6(a). Note that the temporal growth rate intensifies with the increasing value of M when $\text{Re} = 5$ [see top of Fig. 6(b)] but the range of unstable wavenumber slightly decreases with the increasing value of M when $\text{Re} = 40$ [see bottom of Fig. 6(b)]. These facts ensure the long-wave destabilizing and the short-wave stabilizing influences of M on the H mode. Basically, the nontrivial stabilizing effect of M on the H mode in the finite streamwise wavenumber regime can be attributed to the influence of surface tension on the H mode, because the contribution of the

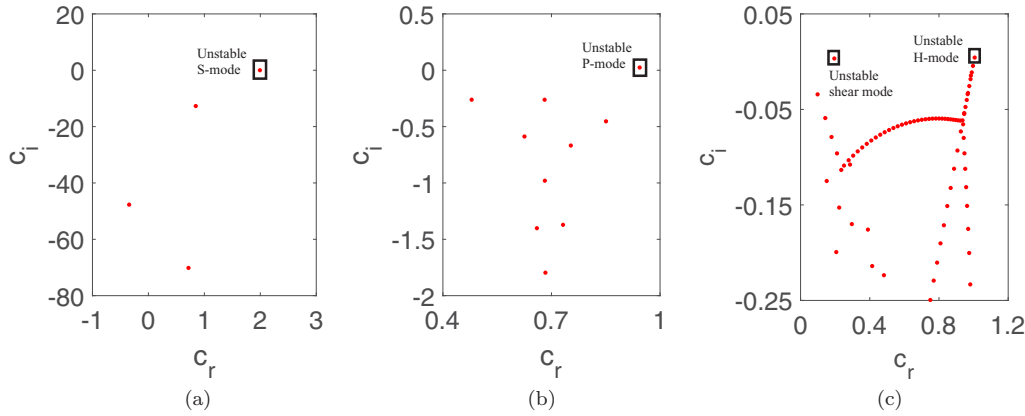


FIG. 5. (a) The eigenvalues in the (c_r, c_i) plane when $Re = 1$, $k_x = 0.05$, and $M = 15$. (b) The eigenvalues in the (c_r, c_i) plane when $Re = 15$, $k_x = 3$, and $M = 20$. (c) The eigenvalues in the (c_r, c_i) plane when $Re = 25000$, $k_x = 0.8$, and $M = 25$. The other parameter values are $Ka = 250$, $\theta = 15^\circ$, $Pr = 7$, $B = 1$, $\beta = 0.02$, and $k_z = 0$.

capillary term k^2We appearing in the normal stress balance equation (45) enhances with the increasing wavenumber k and yields a stabilizing effect. Next we have demonstrated the solo effect of M on the thermocapillary S mode. Figure 7(a) depicts the neutral stability curve in the (Re, k_x) plane for the thermocapillary S mode when the parameter M or, equivalently, the Marangoni number varies. Obviously, the unstable region created by the thermocapillary S mode gradually enhances as long as M increases. In other words, the critical Reynolds number for the S mode beyond which the flow becomes stable due to infinitesimal temperature perturbation increases as long as M increases. Similarly, the unstable range of streamwise wavenumber also magnifies with increasing M . Hence, one can infer that the Marangoni number has a destabilizing influence on the thermocapillary S-mode instability. The favorable impact of M on the thermocapillary S-mode instability can also be found in Fig. 7(b) (top), where the temporal growth rate in the (k_x, ω_i) plane intensifies significantly with the increasing value of M when $Re = 0.1$. This result was previously reported by Ellaban *et al.* [34] for a

falling film over a uniformly heated inclined plane. Furthermore, Fig. 7(b) (bottom) demonstrates the phase speed of the S mode, which reduces with the increasing value of M . Next we have shown the individual effect of M on the thermocapillary P mode. Figure 8(a) displays the neutral stability curve in the (Re, k_x) plane for the thermocapillary P mode when the parameter M varies but the other flow parameters $Ka = 250$, $\theta = 15^\circ$, $Pr = 7$, $B = 1$, $\beta = 0.02$, and $k_z = 0$ are fixed. In this case, the neutral stability curve forms an unstable island shape rather than the unstable open domain found for the H mode when $M = 30$. Obviously, the unstable domain appears in the finite streamwise wavenumber regime instead of the long-wave regime. As long as M decreases, the unstable close domain for the P mode shrinks significantly, and ultimately converts into a point at $M \approx 17.86$. If M is further decreased, the unstable domain completely vanishes. In particular, the thermocapillary P-mode instability does not exist at the low value of M . However, if the parameter M exceeds a critical value $M \approx 17.86$, the unstable island forms and expands with increasing M . Hence, the parameter M or, equivalently, the

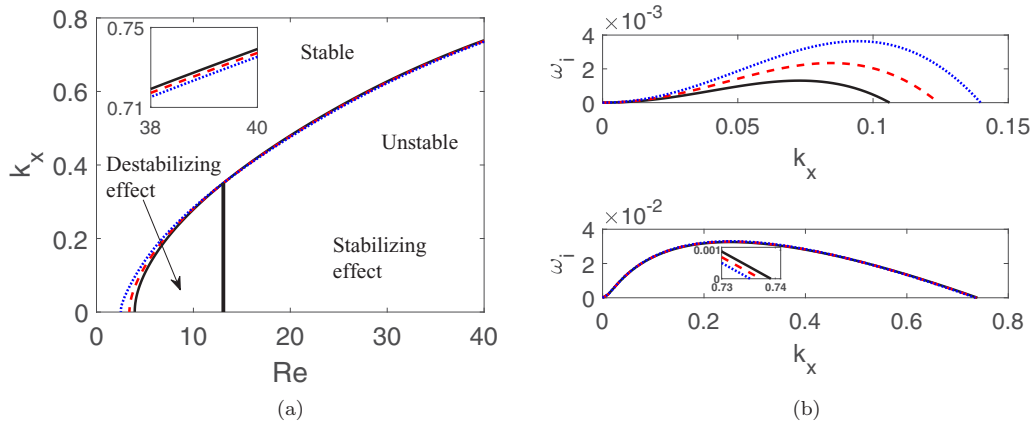


FIG. 6. (a) Variation of the neutral stability curve for the H mode in the (Re, k_x) plane for different values of M or, equivalently, the Marangoni number Ma . Solid, dashed, and dotted lines stand for $M = 6$, $M = 10$, and $M = 14$, respectively. (b) Variation of the temporal growth rate ω_i for the H mode with streamwise wavenumber k_x for different values of M when $Re = 5$ (top) and $Re = 40$ (bottom). Solid, dashed, and dotted lines stand for $M = 6$, $M = 10$, and $M = 14$, respectively. The other parameter values are $Ka = 250$, $\theta = 15^\circ$, $Pr = 7$, $B = 1$, $\beta = 0.02$, and $k_z = 0$.

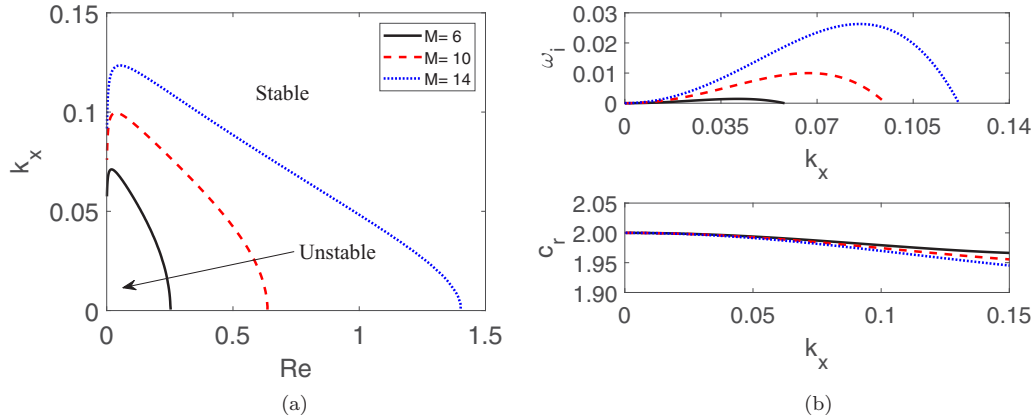


FIG. 7. (a) Variation of the neutral stability curve for the thermocapillary S mode in the (Re, k_x) plane for different values of M or, equivalently, the Marangoni number Ma . Solid, dashed, and dotted lines stand for $M = 6$, $M = 10$, and $M = 14$, respectively. (b) Variation of the temporal growth rate ω_i for the thermocapillary S mode with streamwise wavenumber k_x for different values of M when $Re = 0.1$ (top). Variation of the phase speed c_r for the thermocapillary S mode with streamwise wavenumber k_x for different values of M when $Re = 0.1$ (bottom). Solid, dashed, and dotted lines stand for $M = 6$, $M = 10$, and $M = 14$, respectively. The other parameter values are $Ka = 250$, $\theta = 15^\circ$, $Pr = 7$, $B = 1$, $\beta = 0.02$, and $k_z = 0$.

Marangoni number has a destabilizing effect on the P mode. This result can also be understood from the plot of temporal growth rate illustrated in Fig. 8(b) (top), where the temporal growth rate significantly diminishes, which is followed by the successive reduction of the unstable range of streamwise wavenumber with the decreasing value of M . Figure 8(b) (bottom) displays the associated phase speed for the P mode. Note that the phase speed for the P mode enhances with increasing M as opposed to the result of the S mode. In Fig. 9, we have displayed the neutral stability curve and the temporal growth rate for the shear mode when $Ka = 51000$, $\theta = 1'$, $Pr = 7$, $Bi = 1$, $\beta = 0.02$, and $k_z = 0$. Note that the unstable region forms a tonguelike shape in the neutral diagram. It seems that change in the Marangoni number has a destabilizing impact on the shear mode instability because the critical Reynolds number for the shear mode instability decreases with increas-

ing Ma . Furthermore, the temporal growth rate also enhances with increasing Ma , which is fully consistent with the result shown in Fig. 9(a).

C. Effect of the Biot number

In this section, we investigate the solo effect of the Biot number on different unstable modes found in the numerical simulation. Accordingly, the other flow parameters are kept constant at $Ka = 250$, $\theta = 15^\circ$, $Pr = 7$, $M = 16$, $\beta = 0.02$, and $k_z = 0$. First, we discuss the H-mode and S-mode instabilities. We have noticed that the Biot number or, equivalently, the parameter B has a dual effect on the H-mode instability. The variation of the neutral stability curve for different values of B has been shown in Fig. 10(a). Initially, at the low value of the Biot number ($B \leq 0.5$), the unstable zone induced by the H mode magnifies with the increase in the

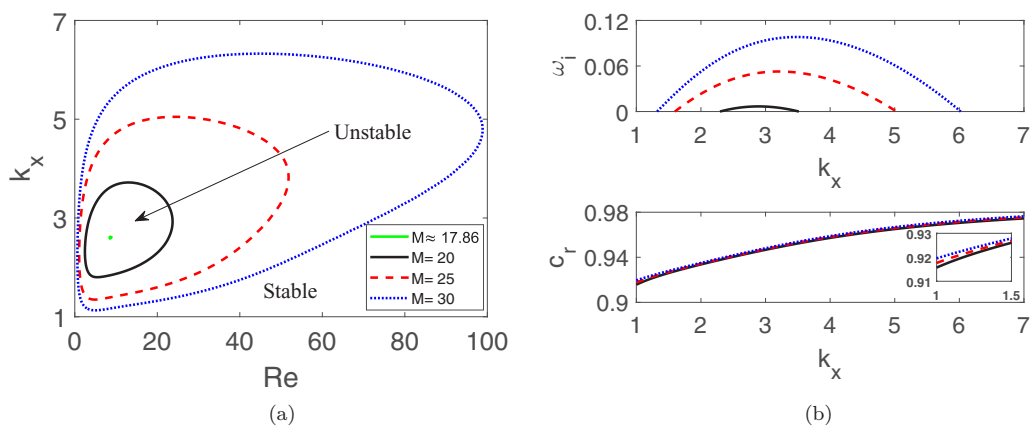


FIG. 8. (a) Variation of the neutral stability curve for the thermocapillary P mode in the (Re, k_x) plane for different values of M or, equivalently, the Marangoni number Ma . Solid, dashed, and dotted lines stand for $M = 20$, $M = 25$, and $M = 30$, respectively. The point appears at $M \approx 17.86$. (b) Variation of the temporal growth rate ω_i for the thermocapillary P mode with streamwise wavenumber k_x for different values of M when $Re = 20$ (top). Variation of the phase speed c_r for the thermocapillary P mode with streamwise wavenumber k_x for different values of M when $Re = 20$ (bottom). Solid, dashed, and dotted lines stand for $M = 20$, $M = 25$, and $M = 30$, respectively. The other parameter values are $Ka = 250$, $\theta = 15^\circ$, $Pr = 7$, $B = 1$, $\beta = 0.02$, and $k_z = 0$.

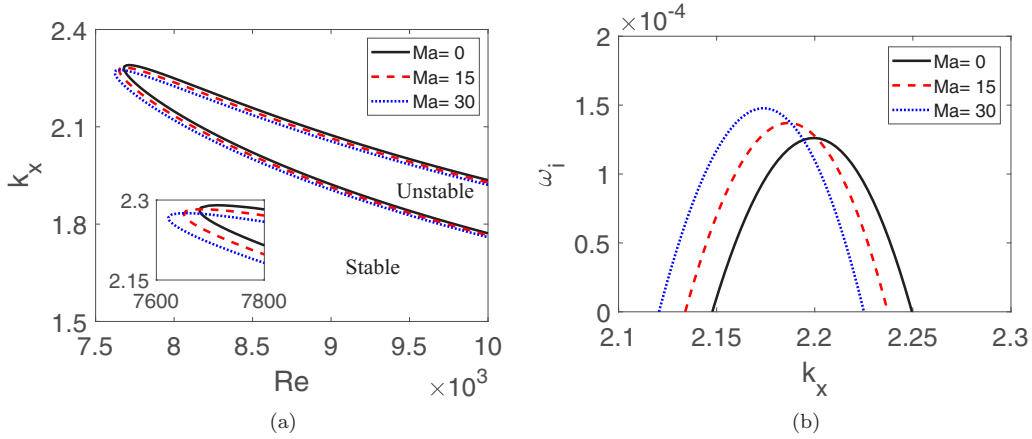


FIG. 9. (a) Variation of the neutral stability curve for the shear mode in the (Re, k_x) plane for different values of the Marangoni number Ma . Solid, dashed, and dotted lines stand for $Ma = 0$, $Ma = 15$, and $Ma = 30$, respectively. (b) Variation of the temporal growth rate ω_i for the shear mode with streamwise wavenumber k_x for different values of Ma when $Re = 8000$. Solid, dashed, and dotted lines stand for $Ma = 0$, $Ma = 15$, and $Ma = 30$, respectively. The other parameter values are $Ka = 51000$, $\theta = 1^\circ$, $Pr = 7$, $Bi = 1$, $\beta = 0.02$, and $k_z = 0$.

value of B close to the onset of instability. But as soon as the Reynolds number increases, the unstable zone created in the finite wavenumber zone reduces marginally with the increasing value of B ($B \leq 0.5$). For further confirmation of these results, we have also plotted the temporal growth rate curve in Fig. 11(a) at two different values of the Reynolds number selected from two different zones. The results reveal that the temporal growth rate increases with increasing B ($B \leq 0.5$) near the onset of instability when $Re = 5$. On the other hand, the unstable range of the streamwise wavenumber reduces in the finite wavenumber regime with increasing B ($B \leq 0.5$) when $Re = 20$. Hence, the parameter B has a destabilizing effect close to the onset of instability but exhibits a stabilizing effect far away from the onset of instability when $B \leq 0.5$. On the contrary, at the high value of the Biot number ($B \geq 1$), the unstable zone induced by the H mode decreases with the increase in the value of B close to the onset of instability. But far away from the onset of instability, a destabilizing effect of B on the H mode is found as the unstable region magnifies

marginally with the increasing value of B [see Fig. 10(b)]. The variation of the temporal growth rate for the H mode with the streamwise wavenumber for two different values of Re is also shown in Fig. 11(b) when $B \geq 1$, which fully supports the result reported in Fig. 10(b). It is evident that the result pertaining to the H mode at the low Biot number ($B \leq 0.5$) is opposite to that of the high Biot number ($B \geq 1$). In particular, the increasing Biot number causes a higher heat transfer at the liquid film surface due to thermal convection. As a result, the liquid film surface becomes cooler and makes the effect of surface tension stronger and results in a stabilizing effect. On the other hand, we have observed a similar effect of the Biot number or, equivalently, the parameter B on the S-mode instability. In particular, at the low value of the Biot number ($B \leq 0.5$), the unstable region induced by the S mode enhances with increasing B [see Fig. 10(a)]. However, the opposite phenomenon takes place at the high value of the Biot number ($B \geq 1$); i.e., the unstable region induced by the S mode reduces with increasing B [see Fig. 10(b)]. The

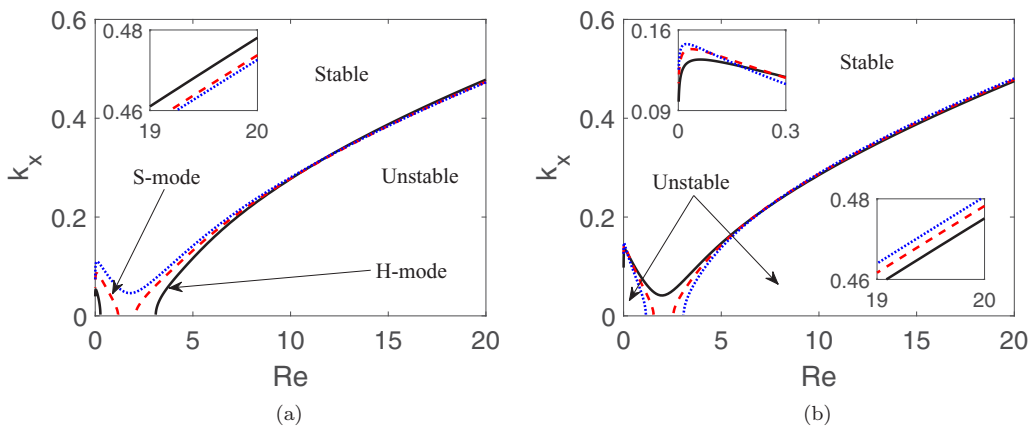


FIG. 10. (a) Variation of the neutral stability curve for the H mode and S mode in the (Re, k_x) plane for different values of B ($B \leq 0.5$) or, equivalently, the Biot number Bi . Solid, dashed, and dotted lines stand for $B = 0.15$, $B = 0.3$, and $B = 0.5$, respectively. (b) Variation of the neutral stability curve for the H mode and S mode in the (Re, k_x) plane for different values of B ($B \geq 1$) or, equivalently, the Biot number Bi . Solid, dashed, and dotted lines stand for $B = 1$, $B = 1.5$, and $B = 2$, respectively. The other parameter values are $Ka = 250$, $\theta = 15^\circ$, $Pr = 7$, $M = 16$, $\beta = 0.02$, and $k_z = 0$.

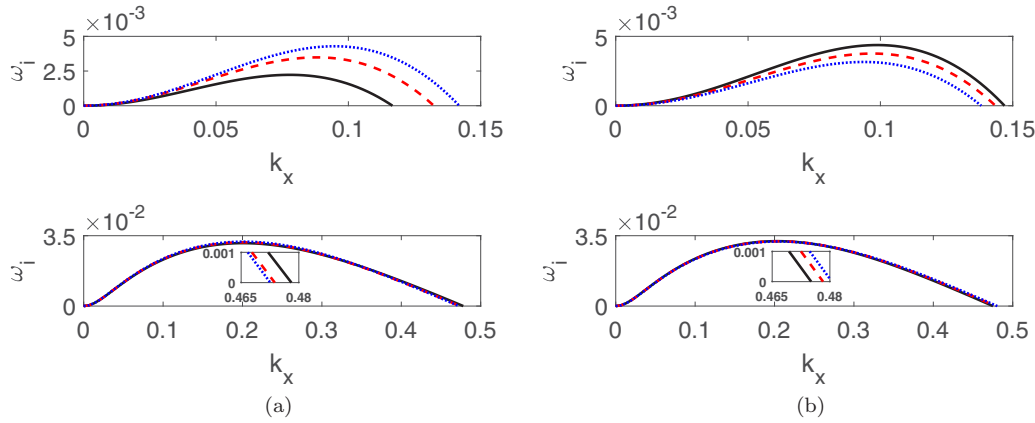


FIG. 11. (a) Variation of the temporal growth rate ω_i for the H mode with streamwise wavenumber k_x for different values of B ($B \leq 0.5$) when $Re = 5$ (top) and $Re = 20$ (bottom). Solid, dashed, and dotted lines stand for $B = 0.15$, $B = 0.3$, and $B = 0.5$, respectively. (b) Variation of the temporal growth rate ω_i for the H mode with streamwise wavenumber k_x for different values of B ($B \geq 1$) when $Re = 5$ (top) and $Re = 20$ (bottom). Solid, dashed, and dotted lines stand for $B = 1$, $B = 1.5$, and $B = 2$, respectively. The other parameter values are $Ka = 250$, $\theta = 15^\circ$, $Pr = 7$, $M = 16$, $\beta = 0.02$, and $k_z = 0$.

above results are further confirmed by plotting the temporal growth rate for the S mode, which is demonstrated in Fig. 12. Obviously, the results of temporal growth rate are in favor of the results predicted from the neutral stability curve shown in Fig. 10. In particular, we have noticed that the temporal growth rate becomes stronger with increasing B when $B \leq 0.5$ [see Fig. 12(a)], but it becomes weaker with increasing B when $B \geq 1$ [see Fig. 12(b)]. Now we discuss the effect of the Biot number on the thermocapillary P mode. As a result, the neutral stability curve pertaining to the P mode is plotted in the (Re, k_x) plane. Figure 13(a) illustrates the neutral stability curve for the P mode when the parameter B varies but the other parameters $Ka = 250$, $\theta = 15^\circ$, $Pr = 7$, $M = 25$, $k_z = 0$, and $\beta = 0.02$ are fixed. Again, the unstable region induced by the P mode forms an island shape, as observed in Fig. 8(a). From the results, it can be clearly seen that the unstable region decreases rapidly with the increase in the value of the Biot

number, and ultimately shrinks into a point at $B \approx 2.71$. If the Biot number is further increased, the P-mode instability disappears. In other words, there exists a critical value of the Biot number ($B \approx 2.71$) above which the unstable island generates due to the P-mode instability. The temporal growth rate and the phase speed associated with the P mode are shown in Fig. 13(b) for different values of the Biot number when $Re = 7$. Obviously, the temporal growth rate decreases with the increase in the value of B , which is followed by the successive reduction of the unstable range of streamwise wavenumber k_x . Hence, one can infer that the Biot number has a stabilizing effect on the P mode. In addition, it is found that the Biot number does not have a significant impact on the shear mode instability (see Fig. 14). Apparently, it seems that the Biot number has a stabilizing effect on the shear mode because the temporal growth rate for the shear mode diminishes with increasing B .

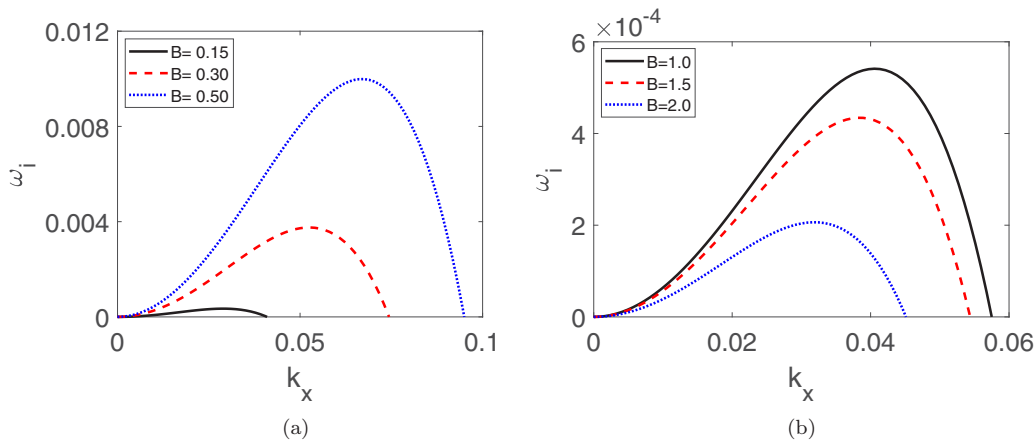


FIG. 12. (a) Variation of the temporal growth rate ω_i for the S mode with streamwise wavenumber k_x for different values of B ($B \leq 0.5$) when $Re = 0.1$. Solid, dashed, and dotted lines stand for $B = 0.15$, $B = 0.30$, and $B = 0.50$, respectively. (b) Variation of the temporal growth rate ω_i for the S mode with streamwise wavenumber k_x for different values of B ($B \geq 1$) when $Re = 0.4$. Solid, dashed, and dotted lines stand for $B = 1$, $B = 1.5$, and $B = 2$, respectively. The other parameter values are $Ka = 250$, $\theta = 15^\circ$, $Pr = 7$, $M = 16$, $\beta = 0.02$, and $k_z = 0$.

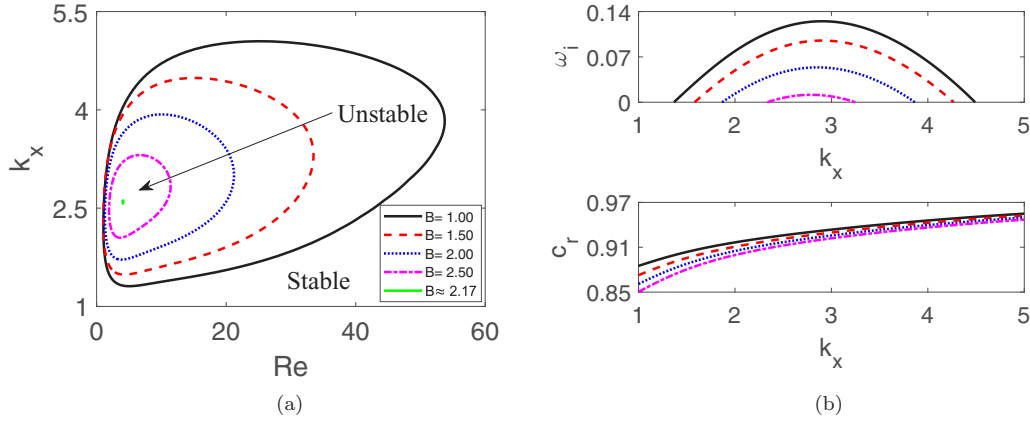


FIG. 13. (a) Variation of the neutral stability curve for the thermocapillary P mode in the (Re, k_x) plane for different values of B or, equivalently, the Biot number Bi . Solid, dashed, dotted, and dash-dotted lines stand for $B = 1, B = 1.5, B = 2,$ and $B = 2.5,$ respectively. The point appears at $B \approx 2.71$. (b) Variation of the temporal growth rate ω_i for the thermocapillary P mode with streamwise wavenumber k_x for different values of B when $Re = 7$ (top). Variation of the phase c_r for the thermocapillary P mode with streamwise wavenumber k_x for different values of B when $Re = 7$ (bottom). Solid, dashed, dotted, and dash-dotted lines stand for $B = 1, B = 1.5, B = 2,$ and $B = 2.5,$ respectively. The other parameter values are $Ka = 250, \theta = 15^\circ, Pr = 7, M = 25, \beta = 0.02,$ and $k_z = 0$.

D. Effect of the slip length

In this section, we deal with the influence of wall slip on different unstable modes found in the numerical simulation. Figure 15(a) reveals the neutral stability curves for the H mode and S mode in the (Re, k_x) plane for different values of the slip length β when $Ka = 250, \theta = 15^\circ, Pr = 7, M = 14.8, B = 1,$ and $k_z = 0$. It is observed that near the onset of instability, the critical Reynolds number for the H mode beyond which the flow becomes unstable decreases with the increase in the value of the slip length and, thereby, the unstable region generated by the H mode magnifies. But at the moderate value of Re , i.e., far away from the onset of instability, the unstable region induced by the H mode reduces with the increase in the value of the slip length. Hence, it can be inferred that, near the threshold of instability, wall slip has a destabilizing effect on the H mode, whereas far away from the threshold of instability, wall slip has a stabilizing effect. In order to reinforce the above

results, the temporal growth rate for the H mode is plotted with respect to the streamwise wavenumber k_x in Fig. 15(b) for two different values of the Reynolds number. At $Re = 4,$ it can be observed that the temporal growth rate for the H mode increases significantly with the rising value of the slip length [see top of Fig. 15(b)]. On the other hand, the maximum temporal growth rate for the H mode decreases slightly as the value of β increases at $Re = 20$ [see bottom of Fig. 15(b)]. A similar type of results pertaining to the slip length on the H mode was previously reported by Samanta *et al.* [32] for an isothermal film falling down a slippery inclined plane. Apparently, it seems that the nonisothermal condition does not change the effect of slip length on the H mode. The variation of the neutral stability curve in the (Re, k_x) plane corresponding to the S-mode instability for different values of β has been revealed in Fig. 15(a). In this case also, we have found a similar effect of β on the S-mode instability. Near the

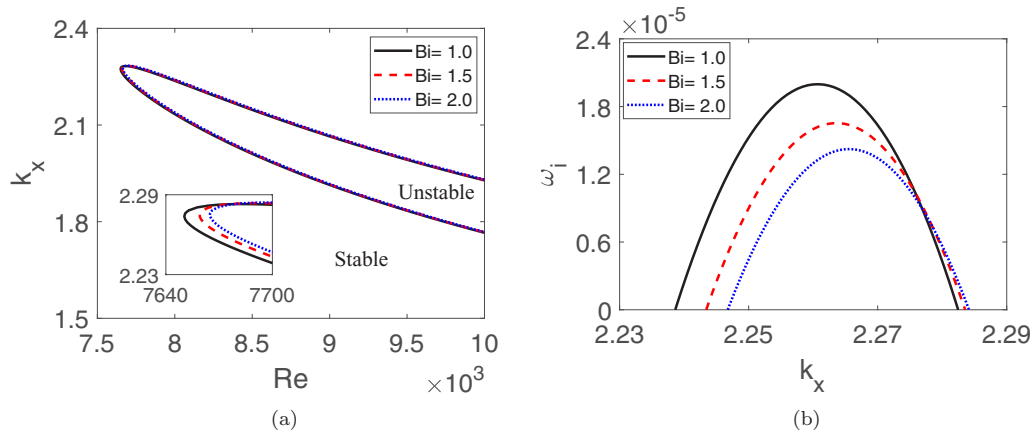


FIG. 14. (a) Variation of the neutral stability curve for the shear mode in the (Re, k_x) plane for different values of the Biot number Bi . Solid, dashed, and dotted lines stand for $Bi = 1, Bi = 1.5,$ and $Bi = 2,$ respectively. (b) Variation of the temporal growth rate ω_i for the shear mode with streamwise wavenumber k_x for different values of Bi when $Re = 7700$. Solid, dashed, and dotted lines stand for $Bi = 1, Bi = 1.5,$ and $Bi = 2,$ respectively. The other parameter values are $Ka = 51000, \theta = 1^\circ, Pr = 7, Bi = 1, \beta = 0.02,$ and $k_z = 0$.

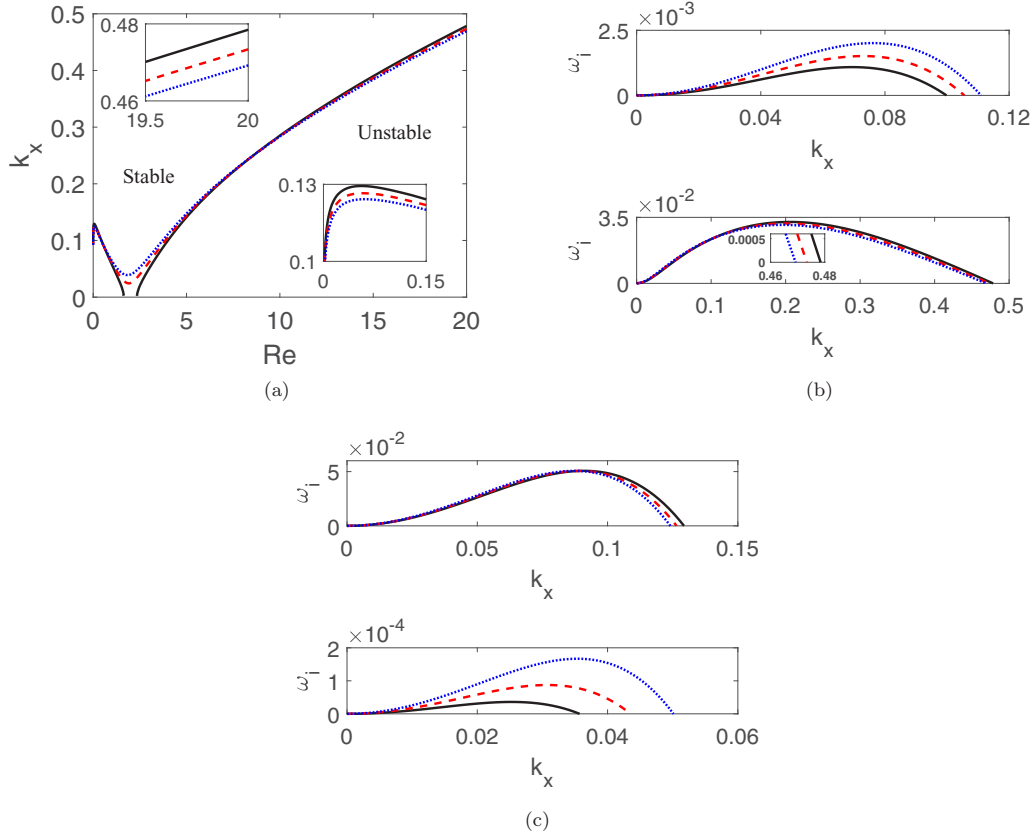


FIG. 15. (a) Variation of the neutral stability curve for the H mode and S mode in the (Re, k_x) plane for different values of the slip length β . Solid, dashed, and dotted lines stand for $\beta = 0$, $\beta = 0.04$, and $\beta = 0.08$, respectively. (b) Variation of the temporal growth rate ω_i for the H mode with streamwise wavenumber k_x for different values of β when $Re = 4$ (top). Variation of the temporal growth rate ω_i for the H mode with streamwise wavenumber k_x for different values of β when $Re = 20$ (bottom). Solid, dashed, and dotted lines stand for $\beta = 0$, $\beta = 0.04$, and $\beta = 0.08$, respectively. (c) Variation of the temporal growth rate ω_i for the S mode with streamwise wavenumber k_x for different values of β when $Re = 0.05$ (top). Variation of the temporal growth rate ω_i for the S mode with streamwise wavenumber k_x for different values of β when $Re = 1.3$ (bottom). Solid, dashed, and dotted lines stand for $\beta = 0$, $\beta = 0.04$, and $\beta = 0.08$, respectively. The other parameter values are $Ka = 250$, $\theta = 15^\circ$, $Pr = 7$, $M = 14.8$, $B = 1$, and $k_z = 0$.

threshold of instability, the unstable region for the S mode increases with increasing β . Consequently, the critical Reynolds number after which the flow becomes stable increases with increasing β . Hence, the wall slip has a destabilizing effect on the S mode. The interesting fact is that the onset of stability for the S mode increases, while the onset of instability for the H mode decreases with increasing β , and finally, both the onsets merge with each other with the higher values of β and generate a single onset of stability. Note that the single onset of stability moves towards the finite streamwise wavenumber regime with increasing β . In addition, we have found that the unstable range of the streamwise wavenumber for the S mode reduces with increasing β at low Reynolds number. To reinforce these results the variation of the temporal growth rate ω_i for the S mode with the streamwise wavenumber k_x for different values of β has been plotted in Fig. 15(c) when $Ka = 250$, $\theta = 15^\circ$, $Pr = 7$, $M = 14.8$, $B = 1$, and $k_z = 0$. The temporal growth rate is found to increase with increasing β at $Re = 1.3$ [see bottom of Fig. 15(c)], while the unstable range of the streamwise wavenumber decreases with increasing β at $Re = 0.05$ [see top of Fig. 15(c)]. Next we have explored the effect of slip length on the P-mode instability. In Fig. 16(a), the variation of the neutral stability curve corresponding to

the thermocapillary P mode is shown for different values of the slip length when $Ka = 250$, $\theta = 15^\circ$, $Pr = 7$, $M = 25$, $B = 1$, and $k_z = 0$. The result indicates that the P-mode instability occurs in the finite wavenumber regime rather than the long-wave regime and forms an islandlike unstable region in the neutral diagram, which gradually magnifies with the increase in the value of the slip length. Hence, it can be concluded that the wall slip has a destabilizing effect on the thermocapillary P mode. Apparently, it seems that the effect of the slip length on the P mode is opposite to the effect of the Biot number on the P mode. To confirm this result, we have also plotted the temporal growth rate with the variation of the streamwise wavenumber at $Re = 40$ in Fig. 16(b) (top) for different values of β . It can be observed that the temporal growth rate enhances with the increase in the value of the slip length, which is followed by the successive increment of the range of k_x . This result is fully consistent with the result reported in Fig. 16(a). Figure 16(b) (bottom) displays the phase speed of the thermocapillary P mode as the slip length varies. Note that the phase speed enhances with the slip length as opposed to the effect of the Biot number on the phase speed for the P mode. Figure 17 depicts the effect of slip length on the shear mode when the slip length β varies. In

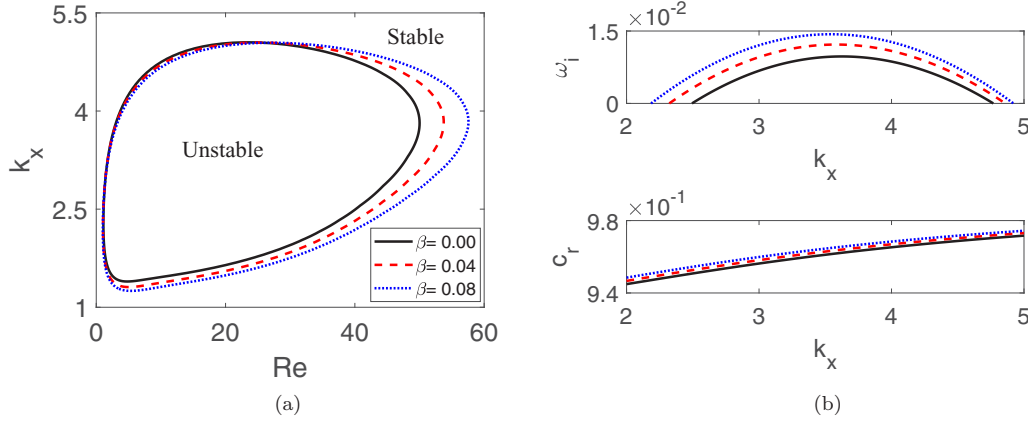


FIG. 16. (a) Variation of the neutral stability curve for the thermocapillary P mode in the (Re, k_x) plane for different values of the slip length. Solid, dashed, and dotted lines stand for $\beta = 0$, $\beta = 0.04$, and $\beta = 0.08$, respectively. (b) Variation of the temporal growth rate ω_i for the thermocapillary P mode with streamwise wavenumber k_x for different values of β when $Re = 40$ (top). Variation of the phase speed c_r for the thermocapillary P mode with streamwise wavenumber k_x for different values of β when $Re = 40$ (bottom). Solid, dashed, and dotted lines stand for $\beta = 0$, $\beta = 0.04$, and $\beta = 0.08$, respectively. The other parameter values are $Ka = 250$, $\theta = 15^\circ$, $Pr = 7$, $M = 25$, $B = 1$, and $k_z = 0$.

the numerical simulation, we have fixed $Ka = 51000$, $\theta = 1'$, $Pr = 7$, $Ma = 15$, $Bi = 1$, $\beta = 0.02$, and $k_z = 0$. The neutral stability curve corresponding to the shear mode has been plotted in Fig. 17(a) for different values of β . In this case, the tongue-like unstable region is created in the neutral diagram, which decreases significantly with the slight increment of β . Hence, it can be inferred that the wall slip has a stabilizing effect on the shear mode instability, as opposed to the result of the Marangoni number on the shear mode. Obviously, the effect of slip length on the shear mode is more prominent than the effect of the Marangoni number. Actually, with the introduction of slip at the impermeable wall, the viscous friction force reduces and causes a stabilizing effect on the shear mode because the viscous friction force is responsible for the generation of the unstable region corresponding to the shear mode. To reinforce the above result, we have also plotted the temporal growth rate with the streamwise wavenumber

in Fig. 17(b) when $Re = 8000$. The result indicates that the temporal growth rate significantly decreases with the increase in the value of the slip length and ensures the destabilizing effect of the slip length.

E. Effect of the Prandtl number

There is evidence that the Prandtl number does not have a significant impact on the different unstable modes except the thermocapillary P mode. For this reason, we focus our attention only on the thermocapillary P mode when the Prandtl number changes. Figure 18(a) illustrates the variation of the neutral stability curve in the (Re, k_x) plane for the thermocapillary P mode when $Ka = 250$, $\theta = 15^\circ$, $M = 25$, $B = 1$, $\beta = 0.02$, and $k_z = 0$. In this case also, the neutral stability curve generates an unstable island with the increasing value

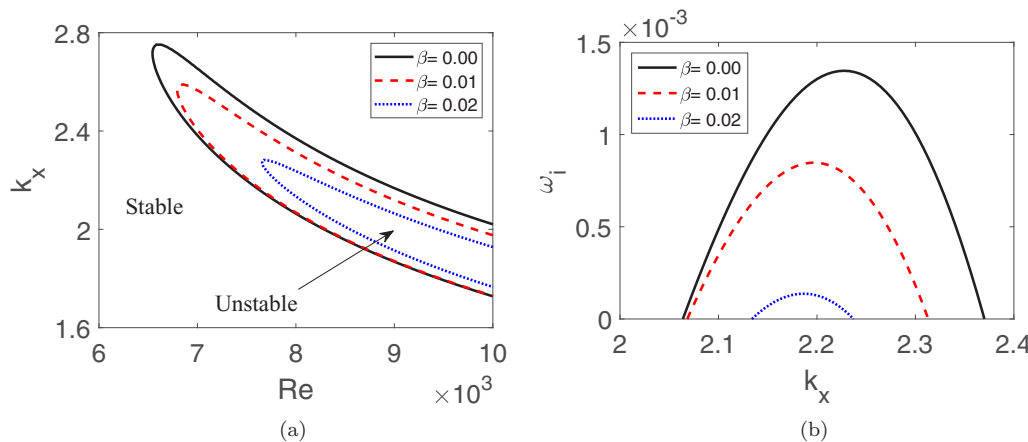


FIG. 17. (a) Variation of the neutral stability curve for the shear mode in the (Re, k_x) plane for different values of the slip length β . Solid, dashed, and dotted lines stand for $\beta = 0$, $\beta = 0.01$, and $\beta = 0.02$, respectively. (b) Variation of the temporal growth rate ω_i for the shear mode with streamwise wavenumber k_x for different values of β when $Re = 8000$. Solid, dashed, and dotted lines stand for $\beta = 0$, $\beta = 0.01$, and $\beta = 0.02$, respectively. The other parameter values are $Ka = 51000$, $\theta = 1'$, $Pr = 7$, $Bi = 1$, $Ma = 15$, and $k_z = 0$.

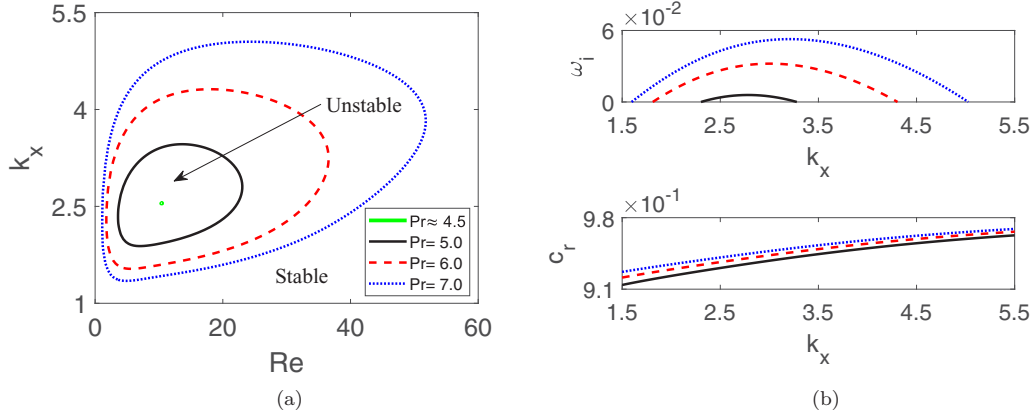


FIG. 18. (a) Variation of the neutral stability curve for the thermocapillary P mode in the (Re, k_x) plane for different values of the Prandtl number. Solid, dashed, and dotted lines stand for $Pr = 5$, $Pr = 6$, and $Pr = 7$, respectively. The point appears at $Pr \approx 4.50$. (b) Variation of the temporal growth rate ω_i for the thermocapillary P mode with streamwise wavenumber k_x for different values of Pr when $Re = 20$ (top). Variation of the phase speed c_r for the thermocapillary P mode with streamwise wavenumber k_x for different values of Pr when $Re = 20$ (bottom). Solid, dashed, and dotted lines stand for $Pr = 5$, $Pr = 6$, and $Pr = 7$, respectively. The other parameter values are $Ka = 250$, $\theta = 15^\circ$, $M = 25$, $B = 1$, $\beta = 0.02$, and $k_z = 0$.

of Pr . In fact, the unstable region forms as soon as the Prandtl number exceeds a critical value. In particular, at the critical value of $Pr \approx 4.50$, the unstable region appears as a point in the (Re, k_x) plane when the streamwise wavenumber is finite. If the Prandtl number is increased, the unstable region expands gradually. Hence, one can infer that the Prandtl number has a destabilizing effect on the P-mode instability. To strengthen the above result, the variation of the temporal growth rate with the streamwise wavenumber is plotted in Fig. 18(b) (top) for different values of the Prandtl number when $Re = 20$. The result is fully in favor of the result of the neutral stability curve depicted in Fig. 18(a) because the temporal growth rate becomes stronger with increasing Pr . Furthermore, the phase speed of the thermocapillary P mode magnifies with increasing Pr [see bottom of Fig. 18(b)].

F. Effect of the spanwise wavenumber

Finally, we have investigated the effect of spanwise wavenumber on the individual unstable modes. First, we have plotted the neutral stability curves for the H mode and S mode in the (Re, k_x) plane for different values of the spanwise wavenumber k_z . The ensuing results can be found in Fig. 19 when $Ka = 250$, $\theta = 15^\circ$, $Pr = 7$, $M = 25$, $B = 1$, and $\beta = 0.02$. The results are produced for two different values of M . In both cases, we have noticed almost a similar scenario as observed in Refs. [55–57]. Note that a single neutral stability curve emerges at the spanwise wavenumber $k_z = 0$. As soon as k_z is increased, the single neutral stability curve turns into a pair of separatrices at $k_z \approx 0.048$, which is illustrated by a dashed line. More specifically, two unstable regions are formed, and both the regions are separated by a single point [see Fig. 19(a)]. In fact, one unstable region is associated with the H mode, while the other unstable region is associated with the S mode. Furthermore, the unstable region induced by the H mode significantly decreases with the increasing value of k_z . Similarly, the unstable region induced by the S mode also decreases with the increasing value of k_z . The important result is

that the unstable region for the H mode gradually shift towards the finite streamwise wavenumber regime with increasing k_z instead of lying in the long-wave regime [58]. However, the unstable region for the S mode gradually shifts towards the long-wave regime with increasing k_z , and ultimately disappears from the neutral diagram approximately at $k_z = 0.18$ [see Fig. 19(a)]. Hence, the spanwise wavenumber has a stabilizing effect on the H-mode and S-mode instabilities. Next we have shown the influence of k_z on the thermocapillary P mode and the shear mode. The results are displayed in Fig. 20. Note that the unstable region for the P mode increases, but the unstable region for the shear mode decreases with the increasing value of the spanwise wavenumber and ensures a destabilizing effect on the P mode but ensures a stabilizing effect on the shear mode. In order to figure out the behavior of individual modes in the (k_x, k_z) plane, the neutral stability curves pertaining to individual unstable modes are revealed in Fig. 21. In this case, the Reynolds number is varied while other flow parameters are kept constant. Note that the unstable domains associated with the H mode, P mode, and shear mode enhance as long as the Reynolds number increases. However, the unstable domain associated with the S mode reduces with the increasing value of the Reynolds number because inertia has a stabilizing effect on the S mode. These results are fully consistent with the results reported in the previous sections.

V. SUMMARY AND CONCLUSIONS

We have investigated a linear stability analysis of a three-dimensional thin viscous incompressible liquid film flowing down a uniformly heated slippery inclined plane. Here the liquid film is flowing under the action of gravitational force. As the plane is uniformly heated, we implement a constant temperature at the plane, while Newton’s law of cooling is implemented to describe the heat transfer due to convection at the film surface. In order to perform the linear stability analysis, we have developed a coupled system of boundary value problems in terms of the amplitudes of perturbation

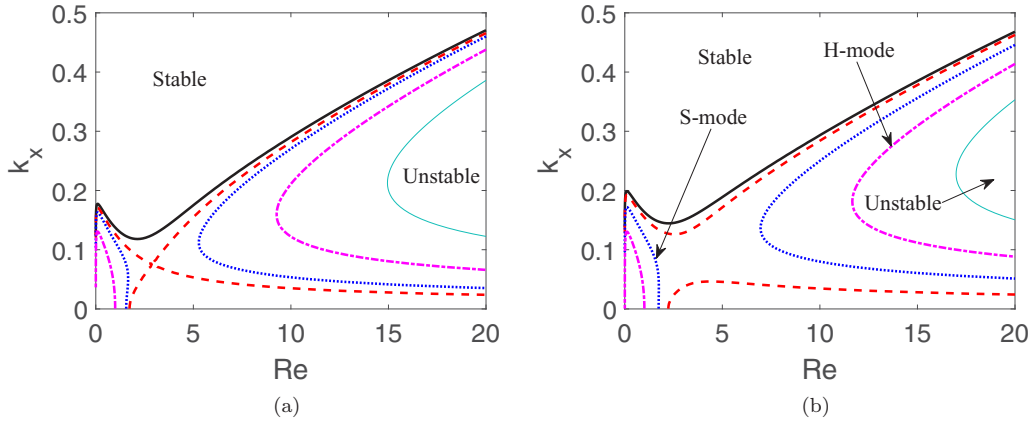


FIG. 19. (a) Variation of the neutral stability curve for the H mode and S mode in the (Re, k_x) plane for different values of the spanwise wavenumber and $M = 25$. Solid, dashed, dotted, dash-dotted, and thin solid lines stand for $k_z = 0, k_z \approx 0.048, k_z = 0.07, k_z = 0.12,$ and $k_z = 0.18$, respectively. (b) Variation of the neutral stability curve for the H mode and S mode in the (Re, k_x) plane for different values of the spanwise wavenumber and $M = 30$. Solid, dashed, dotted, dash-dotted, and thin solid lines stand for $k_z = 0, k_z = 0.05, k_z = 0.1, k_z = 0.15,$ and $k_z = 0.20$, respectively. The other parameter values are $Ka = 250, \theta = 15^\circ, Pr = 7, B = 1,$ and $\beta = 0.02$.

normal velocity and perturbation temperature, respectively, which is in fact a coupled system of a fourth-order differential equation for the perturbation normal velocity and a second-order differential equation for the perturbation temperature. The boundary value problems are solved analytically by using the long-wave series expansion as well as numerically in the arbitrary wavenumber regime by using the Chebyshev spectral collocation method. The analytical solution reveals the existence of three dominant modes, the so-called H mode, S mode, and P mode, in low to moderate values of the Reynolds number. In fact, the H mode emanates due to the streamwise component of the gravitational force, while the S mode and P mode emanate due to the thermocapillary effect. It is found that the threshold of instabilities for the H mode, S mode, and P mode depletes with the increasing value of the slip length and ensures a destabilizing effect.

The numerical solution of the coupled system of boundary value problems reveals that the H-mode instability can be

intensified in the long-wave regime but can be weakened in the finite wavenumber regime with the increasing value of the Marangoni number. On the other hand, the thermocapillary S-mode instability and the finite wavenumber P-mode instability will be stronger if the Marangoni number is increased. Furthermore, we have found that the Biot number exhibits a dual role in the H-mode and S-mode instabilities. More specifically, it exhibits a peculiar behavior on the H mode and S mode. In the long-wave regime, the unstable zones generated by the H mode and S mode increase successively as soon as the Biot number increases, and finally merge with each other with the higher values of the Biot number when $B \leq 0.5$. However, if the Biot number takes a large value, i.e., if $B \geq 1$, the opposite phenomenon happens. In particular, a single neutral stability curve appears at $B = 1$. But, it turns into two neutral stability curves with the increasing value of B . One is associated with the H mode, while the other one is associated with the S mode. It is observed that

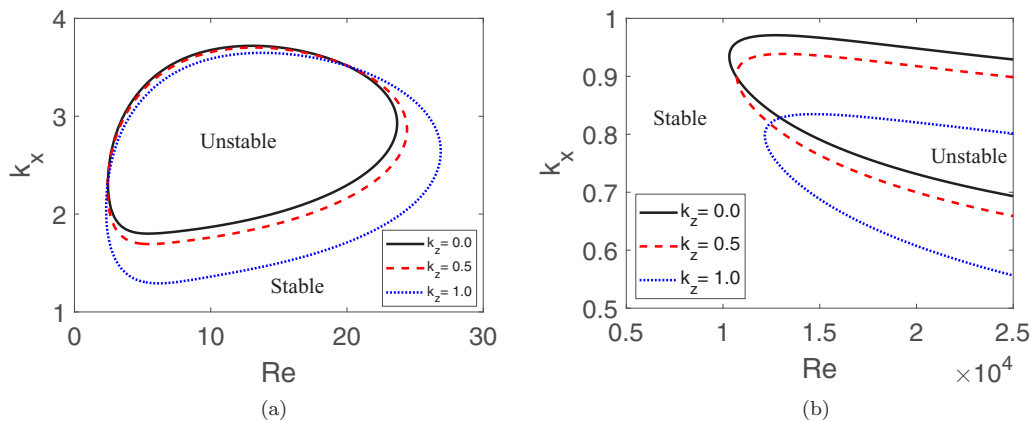


FIG. 20. (a) Variation of the neutral stability curve for the thermocapillary P mode in the (Re, k_x) plane for different values of the spanwise wavenumber. Solid, dashed, and dotted lines stand for $k_z = 0, k_z = 0.5,$ and $k_z = 1$, respectively. The other parameter values are $Ka = 250, \theta = 15^\circ, Pr = 7, M = 20, B = 1,$ and $\beta = 0.02$. (b) Variation of the neutral stability curve for the shear mode in the (Re, k_x) plane for different values of the spanwise wavenumber. Solid, dashed, and dotted lines stand for $k_z = 0, k_z = 0.25,$ and $k_z = 0.5$, respectively. The other parameter values are $Ka = 13000, \theta = 1^\circ, Pr = 7, Ma = 30, Bi = 1,$ and $\beta = 0.02$.

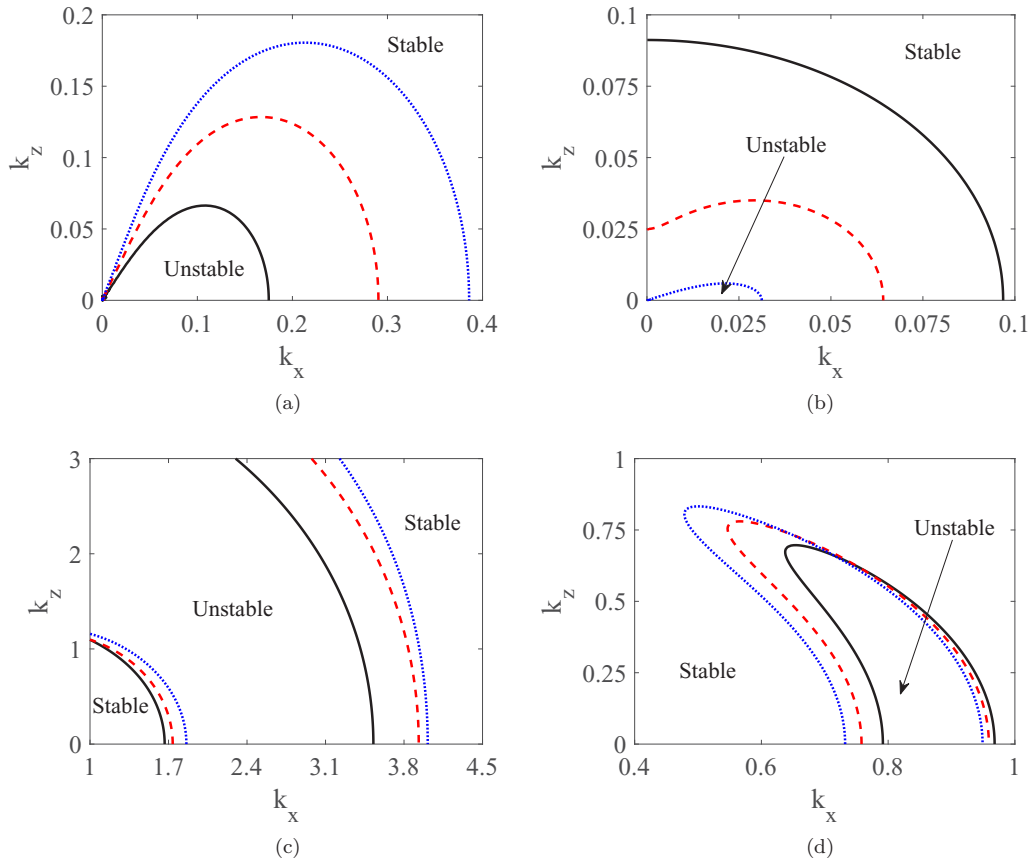


FIG. 21. (a) Variation of the neutral stability curve for the H mode in the (k_x, k_z) plane for different values of the Reynolds number. Solid, dashed, and dotted lines stand for $Re = 5$, $Re = 10$, and $Re = 15$, respectively. The other parameter values are $Ka = 250$, $\theta = 15^\circ$, $Pr = 7$, $M = 25$, $B = 1$, and $\beta = 0.02$. (b) Variation of the neutral stability curve for the S mode in the (k_x, k_z) plane for different values of the Reynolds number. Solid, dashed, and dotted lines stand for $Re = 0.4$, $Re = 0.8$, and $Re = 1.2$, respectively. The other parameter values are $Ka = 250$, $\theta = 15^\circ$, $Pr = 7$, $M = 14$, $B = 1$, and $\beta = 0.02$. (c) Variation of the neutral stability curve for the P mode in the (k_x, k_z) plane for different values of the Reynolds number. Solid, dashed, and dotted lines stand for $Re = 5$, $Re = 10$, and $Re = 15$, respectively. The other parameter values are $Ka = 250$, $\theta = 15^\circ$, $Pr = 7$, $M = 21$, $B = 1$, and $\beta = 0.02$. (d) Variation of the neutral stability curve for the shear mode in the (k_x, k_z) plane for different values of the Reynolds number. Solid, dashed, and dotted lines stand for $Re = 15000$, $Re = 17500$, and $Re = 20000$, respectively. The other parameter values are $Ka = 13000$, $\theta = 1^\circ$, $Pr = 7$, $Ma = 30$, $Bi = 1$, and $\beta = 0.02$.

two unstable zones decrease gradually with the increasing value of B . Moreover, the P-mode instability emanates in the finite streamwise wavenumber regime when the parameter B exceeds a critical value and magnifies with increasing B . Hence, the Biot number has a stabilizing effect on the P-mode instability. Apparently, it seems that the Biot number does not have a significant influence on the shear mode. The numerical simulation of the coupled system of boundary value problems also demonstrates that the slip length has a destabilizing effect on the H mode and S mode as observed in the analytical calculation because the unstable regions induced by the H mode and S mode magnify with the increasing value of the slip length. In this case also, the onset of instability for the H mode and the onset of stability for the S mode merge with each other and form a single neutral stability curve as long as the slip length increases. Furthermore, the onset of stability shifts towards the finite streamwise wavenumber regime with increasing β . We have noted that the Prandtl number has no significant influence on the H mode, S mode, and shear mode, but the P mode becomes more unstable with the increasing value of the Prandtl number. In fact, the unstable region ap-

pears when the Prandtl number exceeds a critical value and expands significantly as long as the Prandtl number increases. Finally, the effect of spanwise wavenumber is explored on the different unstable modes. It is found that the unstable regions generated by the H mode, S mode, and shear mode decrease with the increasing value of the spanwise wavenumber. However, the opposite event happens in the case of the P mode, where the P-mode instability intensifies as long as the spanwise wavenumber increases.

ACKNOWLEDGMENTS

The authors would like to thank the anonymous referees for their suggestions on improving the manuscript.

APPENDIX A: SQUIRE’S TRANSFORMATION FOR NONISOTHERMAL FLOW CONFIGURATION

This Appendix deals with Squire’s transformation for the nonisothermal flow configuration. Using the normal node

solution (40), the linearized three-dimensional perturbation equations (29)–(39) can be rewritten as

$$ik_x \hat{u} + \partial_y \hat{v} + ik_z \hat{w} = 0, \quad 0 \leq y \leq 1, \quad (A1)$$

$$\begin{aligned} & \text{Re}[(\bar{U} - c)ik_x \hat{u} + \partial_y \bar{U} \hat{v}] \\ & = -2ik_x \hat{p} + [\partial_{yy} \hat{u} - (k_x^2 + k_z^2) \hat{u}], \quad 0 \leq y \leq 1, \end{aligned} \quad (A2)$$

$$\begin{aligned} & \text{Re}(\bar{U} - c)ik_x \hat{v} \\ & = -2\partial_y \hat{p} + [\partial_{yy} \hat{v} - (k_x^2 + k_z^2) \hat{v}], \quad 0 \leq y \leq 1, \end{aligned} \quad (A3)$$

$$\begin{aligned} & \text{Re}(\bar{U} - c)ik_x \hat{w} \\ & = -2ik_z \hat{p} + [\partial_{yy} \hat{w} - (k_x^2 + k_z^2) \hat{w}], \quad 0 \leq y \leq 1, \end{aligned} \quad (A4)$$

$$\begin{aligned} & \text{Pe}[(\bar{U} - c)ik_x \hat{\tau} + \partial_y \bar{T} \hat{v}] \\ & = [\partial_{yy} \hat{\tau} - (k_x^2 + k_z^2) \hat{\tau}], \quad 0 \leq y \leq 1, \end{aligned} \quad (A5)$$

$$\hat{u} = \beta \partial_y \hat{u}, \quad \hat{v} = 0, \quad \hat{w} = \beta \partial_y \hat{w}, \quad \hat{T} = 0, \quad \text{at } y = 0, \quad (A6)$$

$$\begin{aligned} \partial_y \hat{u} + ik_x \hat{v} - \frac{2\hat{h}}{1+2\beta} & = -2\text{Ma} \left[ik_x \hat{\tau} - \frac{\text{Bi}}{1+\text{Bi}} ik_x \hat{h} \right], \\ & \text{at } y = 1, \end{aligned} \quad (A7)$$

$$\partial_y \hat{w} + ik_z \hat{v} = -2\text{Ma} \left[ik_z \hat{\tau} - \frac{\text{Bi}}{1+\text{Bi}} ik_z \hat{h} \right], \quad \text{at } y = 1, \quad (A8)$$

$$\begin{aligned} -\hat{p} + \frac{\cot \theta}{1+2\beta} \hat{h} + \partial_y \hat{v} & = - \left[\text{We} - \frac{\text{Ma}}{1+\text{Bi}} \right] \\ & \times (k_x^2 + k_z^2) \hat{h}, \quad \text{at } y = 1, \end{aligned} \quad (A9)$$

$$\partial_y \hat{\tau} = \text{Bi} \left[\frac{\text{Bi}}{1+\text{Bi}} \hat{h} - \hat{\tau} \right], \quad \text{at } y = 1, \quad (A10)$$

$$(\bar{U} - c)ik_x \hat{h} = \hat{v}, \quad \text{at } y = 1. \quad (A11)$$

Now we apply the following extended form of Squire’s transformations [58]:

$$\left. \begin{aligned} k_x \hat{u} + k_z \hat{w} & = k\tilde{u}, \quad \hat{v} = \tilde{v}, \quad k_x^2 + k_z^2 = k^2, \quad \hat{p} = \tilde{p}, \\ c & = \tilde{c}, \quad k_x \hat{\tau} = k\tilde{\tau}, \quad k_x \hat{h} = k\tilde{h}, \quad k \cot \theta = k_x \cot \tilde{\theta}, \\ k_x \text{Re} & = k\tilde{\text{Re}}, \quad k_x \text{Pe} = k\tilde{\text{Pe}}, \quad k \text{We} = k_x \tilde{\text{We}}, \\ k \text{Ma} & = k_x \tilde{\text{Ma}}, \quad \text{Bi} = \tilde{\text{Bi}}. \end{aligned} \right\} \quad (A12)$$

Using the above transformations (A12), the three-dimensional perturbation equations (A1)–(A11) can be converted into equivalent two-dimensional perturbation equations:

$$ik\tilde{u} + \partial_y \tilde{v} = 0, \quad 0 \leq y \leq 1, \quad (A13)$$

$$\begin{aligned} & \tilde{\text{Re}}[(\bar{U} - \tilde{c})ik\tilde{u} + \partial_y \bar{U} \tilde{v}] \\ & = -2ik\tilde{p} + [\partial_{yy} \tilde{u} - k^2 \tilde{u}], \quad 0 \leq y \leq 1, \end{aligned} \quad (A14)$$

$$\begin{aligned} & \tilde{\text{Re}}[(\bar{U} - \tilde{c})ik\tilde{v}] \\ & = -2\partial_y \tilde{p} + [\partial_{yy} \tilde{v} - k^2 \tilde{v}], \quad 0 \leq y \leq 1, \end{aligned} \quad (A15)$$

$$\begin{aligned} & \tilde{\text{Pe}}[(\bar{U} - \tilde{c})ik\tilde{\tau} + \partial_y \bar{T} \tilde{v}] \\ & = [\partial_{yy} \tilde{\tau} - k^2 \tilde{\tau}], \quad 0 \leq y \leq 1, \end{aligned} \quad (A16)$$

$$\tilde{u} = \beta \partial_y \tilde{u}, \quad \tilde{v} = 0, \quad \tilde{\tau} = 0, \quad \text{at } y = 0, \quad (A17)$$

$$\begin{aligned} \partial_y \tilde{u} + ik\tilde{v} - \frac{2\tilde{h}}{1+2\beta} & = -2\tilde{\text{Ma}} \left[ik\tilde{\tau} - \frac{\tilde{\text{Bi}}}{1+\tilde{\text{Bi}}} ik\tilde{h} \right], \\ & \text{at } y = 1, \end{aligned} \quad (A18)$$

$$\begin{aligned} & -\tilde{p} + \frac{\cot \tilde{\theta}}{1+2\beta} \tilde{h} + \partial_y \tilde{v} \\ & = - \left[\tilde{\text{We}} - \frac{\tilde{\text{Ma}}}{1+\tilde{\text{Bi}}} \right] k^2 \tilde{h}, \quad \text{at } y = 1, \end{aligned} \quad (A19)$$

$$\partial_y \tilde{\tau} = \tilde{\text{Bi}} \left[\frac{\tilde{\text{Bi}}}{1+\tilde{\text{Bi}}} \tilde{h} - \tilde{\tau} \right], \quad \text{at } y = 1, \quad (A20)$$

$$(\bar{U} - \tilde{c})ik\tilde{h} = \tilde{v}, \quad \text{at } y = 1, \quad (A21)$$

where tilde quantities are the parameters for the two-dimensional nonisothermal flow configuration. From the above transformation, we note that $\tilde{\text{Re}} = (k_x/k)\text{Re}$, which implies that $\tilde{\text{Re}} < \text{Re}$ as $k_z \neq 0$ for the three-dimensional disturbance. Therefore, we can conclude that the primary instability corresponding to the two-dimensional disturbance initiates at a lower Reynolds number than that of the three-dimensional disturbance.

APPENDIX B: SOLUTION OF FIRST-ORDER LONG-WAVE EQUATIONS

$$\begin{aligned} \phi_1(y) & = i \left[\frac{2(d_0 + d_1 \text{Re})y + (d_0 + d_1 \text{Re})\beta y^2}{6(1+\text{Bi})^2(1+2\beta)^2} \right. \\ & \left. + d_2 y^3 + d_3 y^4 + d_4 y^5 \right], \end{aligned} \quad (B1)$$

$$\begin{aligned} \tau_1(y) & = \frac{\text{Bi}}{(1+\text{Bi})^2} \left[\frac{e_0 y}{30(1+\text{Bi})} + e_1 y^3 \right. \\ & \left. + e_2 y^4 + e_3 y^5 \right], \end{aligned} \quad (B2)$$

where

$$\begin{aligned} d_0 & = -6\beta(1+2\beta)[- \text{BiMa}(1+2\beta)\eta_0 + i(1+\text{Bi})^2\eta_1 \\ & \quad + (1+\text{Bi})^2\eta_0 \cot \theta], \\ d_1 & = (1+\text{Bi})^2[3c_0(1+2\beta)^2 - 2(1+4\beta+6\beta^2)]\eta_0, \\ d_2 & = \frac{\eta_0[\text{Re}\beta\{c_0 + 2(c_0 - 1)\beta - (1+2\beta)\cot \theta\}]}{3(1+2\beta)^2}, \\ d_3 & = \frac{\text{Re}[c_0 + 2(c_0 - 1)\beta]\eta_0}{12(1+2\beta)^2}, \quad d_4 = \frac{\text{Re}(1+\beta)\eta_0}{30(1+2\beta)^2}, \\ e_0 & = \frac{i\text{Pe}(-10 - 25\text{Bi} - 6\text{Bi}^2 + 15\text{Bi}c_0 + 5\text{Bi}^2c_0)}{1+2\beta} \\ & \quad + \frac{10(3+\text{Bi})\{\text{Bi}(c_0 - 2) - 1\}\beta\eta_0}{1+2\beta} + 30\text{Bi}(1+\text{Bi})\eta_1, \\ e_1 & = \frac{i\text{Pe}[\text{Bi}\{c_0 + 2(c_0 - 2)\beta\} - 2\beta]\eta_0}{6(1+2\beta)}, \\ e_2 & = \frac{i(1+3\text{Bi})\text{Pe}\eta_0}{12(1+2\beta)}, \quad e_3 = -\frac{i\text{Bi}\text{Pe}\eta_0}{20(1+2\beta)}. \end{aligned}$$

APPENDIX C: EXPRESSIONS OF THE COEFFICIENTS FOR c_3

$$\begin{aligned}
 h_0 &= 6720(1 + \text{Bi})^5[5\text{We}\{1 + \beta(5 + 6\beta)\} - 3\{3 + 5\beta(3 + 4\beta)\} \cot \theta], \\
 h_1 &= (1 + \text{Bi})[\text{Bi}\{16800\text{Bi}(5 + 3\text{Bi}) + (5435 - \text{Bi}(2090 + 749\text{Bi}))\text{Pe}^2\} - 40\text{Bi}\{(\text{Bi}(28 + 31\text{Bi}) - 619)\text{Pe}^2 \\
 &\quad - 840(3 + \text{Bi}(19 + 11\text{Bi}))\}\beta + 4480\{15(1 + \text{Bi})(2\text{Bi}(6 + 7\text{Bi}) - 3) + \text{Bi}(6 + \text{Bi})\text{Pe}^2\}\beta^2 \\
 &\quad + 806400\text{Bi}(1 + \text{Bi})^2\beta^3 - 33600(1 + 5\beta) + 280\text{BiPe}(1 + \text{Bi})(1 + 2\beta)(7\text{Bi} - 120\beta - 33) \cot \theta], \\
 h_2 &= 4200\text{Pe}(\text{Bi} - 8\beta - 3)(\text{Bi} + 2\text{Bi}\beta)^2, \\
 h_3 &= 5(\text{Bi} + 1)^4 \csc^2 \theta [\{8\beta(252\beta(5\beta(12\beta + 23) + 82) + 6617) + 6617\} \cos(2\theta) \\
 &\quad - 8\beta\{252\beta(5\beta(12\beta + 25) + 92) + 7513\} - 7513], \\
 h_4 &= \text{Bi}(1 + \text{Bi})[\text{Pe}\{3653\text{Bi} - 9605 + 2\text{Bi}\beta(10649 + 40\beta(536 + 343\beta))\} - 10\beta\{8317 + 8\beta(3419 + 7\beta(703 + 360\beta))\} \\
 &\quad + 280(1 + \text{Bi})(1 + 2\beta)\{49 + \beta(343 + 120\beta(7 + 6\beta))\} \cot \theta], \\
 h_5 &= -21000\text{Bi}^2(1 + 2\beta)^3\{5 + 4\beta(5 + 6\beta)\}, \\
 h_6 &= 495\text{BiMa}(1 + 2\beta)[13535 + 2\beta\{67675 + 8\beta(34983 + 70\beta(1045 + 216\beta(5 + 2\beta)))\}] \\
 &\quad - 256(1 + \text{Bi})^2[17363 + 11\beta\{17363 + 30\beta(2609 + 63\beta(94 + 15\beta(7 + 3\beta)))\} \cot \theta], \\
 h_7 &= 16(1 + \beta)[75872 + 13\beta\{75872 + 11\beta(38692 + 15\beta(7888 + 21\beta(652 + 75\beta(8 + 3\beta))))\}].
 \end{aligned}$$

APPENDIX D: PADÉ APPROXIMATION OF THE LONG-WAVE SOLUTIONS

Following the works of Lange *et al.* [59] and Pal and Samanta [60], the Padé approximation is applied to improve the result obtained from the third-order long-wave solution when the wavenumber $k_x \rightarrow 0$. To this end, the complex wave speed c for the H mode is expressed as a ratio of two polynomials in terms of wavenumber $k_x = k$ ($k_z = 0$),

$$c = \frac{P(k)}{Q(k)}, \tag{D1}$$

where

$$\begin{aligned}
 P(k) &= p_0 + p_1k + p_2k^2 + \dots + p_ik^i, \\
 Q(k) &= 1 + q_1k + q_2k^2 + \dots + q_jk^j \neq 0,
 \end{aligned}$$

where the unknown coefficients p_0, p_1, \dots, p_i and q_1, \dots, q_j are determined analytically by using the long-wave solution.

[1] K. Huang, Y. Hu, and X. Deng, Experimental study on heat and mass transfer of falling liquid films in converging-diverging tubes with water, *Int. J. Heat Mass Transfer* **126**, 721 (2018).

[2] P. D. Frisk and E. J. Davis, The enhancement of heat transfer by waves in stratified gas-liquid flow, *Int. J. Heat Mass Transfer* **15**, 1537 (1972).

[3] N. Brauner and D. M. Maron, Characteristics of inclined thin films, waviness and the associated mass transfer, *Int. J. Heat Mass Transfer* **25**, 99 (1982).

[4] P. L. Kapitza and S. P. Kapitza, Wave flow of thin fluid layers of liquid, *Zh. Eksp. Teor. Fiz.* **19**, 105 (1949).

[5] S. V. Alekseenko, V. Y. Nakoryakov, and B. G. Pokusaev, Wave formation on a vertical falling liquid film, *AIChE J.* **31**, 1446 (1985).

[6] H. C. Chang, Wave evolution on a falling film, *Annu. Rev. Fluid Mech.* **42**, 1553 (1994).

[7] J. Liu and J. P. Gollub, Solitary wave dynamics of film flows, *Phys. Fluids* **6**, 1702 (1994).

[8] R. V. Craster and O. K. Matar, Dynamics and stability of thin liquid films, *Rev. Mod. Phys.* **81**, 1131 (2009).

[9] T. B. Benjamin, Wave formation in laminar flow down an inclined plane, *J. Fluid Mech.* **2**, 554 (1957).

[10] C. S. Yih, Stability of liquid flow down an inclined plane, *Phys. Fluids* **6**, 321 (1963).

[11] S. P. Lin, Instability of a liquid film flowing down an inclined plane, *Phys. Fluids* **10**, 308 (1967).

[12] G. J. De Bruin, Stability of a layer of liquid flowing down an inclined plane, *J. Eng. Math.* **8**, 259 (1974).

[13] R. Chin, F. Abernathy, and J. Bertschy, Gravity and shear wave stability of free surface flows. Part I. Numerical calculations, *J. Fluid Mech.* **168**, 501 (1986).

[14] J. M. Floryan, S. H. Davis, and R. E. Kelly, Instabilities of a liquid film flowing down a slightly inclined plane, *Phys. Fluids* **30**, 983 (1987).

[15] S. P. Lin, Stability of liquid flow down a heated inclined plane, *Lett. Heat Mass Transfer* **2**, 361 (1975).

[16] S. Sreenivasan and S. P. Lin, Surface tension driven instability of a liquid film flow down a heated incline, *Int. J. Heat Mass Transfer* **21**, 1517 (1978).

[17] M. K. Smith, The long-wave instability in heated or cooled inclined liquid layers, *J. Fluid Mech.* **219**, 337 (1990).

[18] D. A. Goussis and R. E. Kelly, Surface wave and thermocapillary instabilities in a liquid film flow, *J. Fluid Mech.* **223**, 25 (1991).

- [19] S. W. Joo, S. H. Davis, and S. G. Bankoff, Long-wave instabilities of heated falling films: Two-dimensional theory of uniform layers, *J. Fluid Mech.* **230**, 117 (1991).
- [20] S. W. Joo, S. H. Davis, and S. G. Bankoff, A mechanism for rivulet formation in heated falling films, *J. Fluid Mech.* **321**, 279 (1996).
- [21] C. Ruyer-Quil, B. Scheid, S. Kalliadasis, M. G. Velarde, and R. K. Zeytounian, Thermocapillary long waves in a liquid film flow. Part 1. Low-dimensional formulation, *J. Fluid Mech.* **538**, 199 (2005).
- [22] B. Scheid, C. Ruyer-Quil, S. Kalliadasis, M. G. Velarde, and R. K. Zeytounian, Thermocapillary long waves in a liquid film flow. Part 2. Linear stability and nonlinear waves, *J. Fluid Mech.* **538**, 223 (2005).
- [23] J. Hu, H. B. Hadid, D. Henry, and A. Mojtabi, Linear temporal and spatiotemporal stability analysis of a binary liquid film flowing down an inclined uniformly heated plate, *J. Fluid Mech.* **599**, 269 (2008).
- [24] A. Samanta, Stability of inertialess liquid film flowing down a heated inclined plane, *Phys. Lett. A* **372**, 6653 (2008).
- [25] L. A. Dávalos-Orozco, The effect of the thermal conductivity and thickness of the wall on the nonlinear instability of a thin film flowing down an incline, *Int. J. Nonlinear Mech.* **47**, 1 (2012).
- [26] L. A. Dávalos-Orozco, Stability of thin liquid films falling down isothermal and non-isothermal walls, *Interfacial Phenom. Heat Transfer* **1**, 93 (2013).
- [27] T. D. Blake, Slip between a liquid and a solid: D.M. Tolstoi's (1952) theory reconsidered, *Colloids Surf.* **47**, 135 (1990).
- [28] C. Neto, D. R. Evans, E. Bonaccorso, H. J. Butt, and V. S. J. Craig, Boundary slip in Newtonian liquids: A review of experimental studies, *Rep. Prog. Phys.* **68**, 2859 (2005).
- [29] J. P. Pascal, Linear stability of fluid flow down a porous inclined plane, *J. Phys. D: Appl. Phys.* **32**, 417 (1999).
- [30] G. S. Beavers and D. D. Joseph, Boundary conditions at a naturally permeable wall, *J. Fluid Mech.* **30**, 197 (1967).
- [31] P. G. Saffman, On the boundary condition at the surface of a porous medium, *Stud. Appl. Math.* **50**, 93 (1971).
- [32] A. Samanta, C. Ruyer-Quil, and B. Goyeau, A falling film down a slippery inclined plane, *J. Fluid Mech.* **684**, 353 (2011).
- [33] Z. Ding and T. N. Wong, Falling liquid films on a slippery substrate with Marangoni effects, *Int. J. Heat Mass Transfer* **90**, 689 (2015).
- [34] E. Ellaban, J. P. Pascal, and S. J. D. D'Alessio, Instability of a binary liquid film flowing down a slippery heated plate, *Phys. Fluids* **29**, 092105 (2017).
- [35] U. Thiele, B. Goyeau, and M. G. Velarde, Stability analysis of thin film flow along a heated porous wall, *Phys. Fluids* **21**, 014103 (2009).
- [36] I. M. R. Sadiq, R. Usha, and S. W. Joo, Instabilities in a liquid film flow over an inclined heated porous substrate, *Chem. Eng. Sci.* **65**, 4443 (2010).
- [37] K. A. Ogden, S. J. D. D'Alessio, and J. P. Pascal, Gravity-driven flow over heated, porous, wavy surfaces, *Phys. Fluids* **23**, 122102 (2011).
- [38] F. A. Bhat and A. Samanta, Linear stability of a contaminated fluid flow down a slippery inclined plane, *Phys. Rev. E* **98**, 033108 (2018).
- [39] S. Kalliadasis, C. Ruyer-Quil, B. Scheid, and M. G. Velarde, *Falling Liquid Films* (Springer, Berlin, 2012).
- [40] D. Goussis and R. Kelly, On the thermocapillary instabilities in a liquid layer heated from below, *Int. J. Heat Mass Transfer* **33**, 2237 (1990).
- [41] S. Miladinova, S. Slavtchev, G. Lebon, and J. C. Legros, Long-wave instabilities of non-uniformly heated falling films, *J. Fluid Mech.* **453**, 153 (2002).
- [42] A. Samanta, Stability of liquid film falling down a vertical non-uniformly heated wall, *Physica D* **237**, 2587 (2008).
- [43] I. M. R. Sadiq and R. Usha, Thin Newtonian film flow down a porous inclined plane: Stability analysis, *Phys. Fluids* **20**, 022105 (2008).
- [44] W. A. Rowin and S. Ghaemi, Streamwise and spanwise slip over a superhydrophobic surface, *J. Fluid Mech.* **870**, 1127 (2019).
- [45] A. Samanta, Non-modal stability analysis in viscous fluid flows with slippery walls, *Phys. Fluids* **32**, 064105 (2020).
- [46] R. S. Voronov, D. V. Papavassiliou, and L. L. Lee, Review of fluid slip over superhydrophobic surfaces and its dependence on the contact angle, *Ind. Eng. Chem. Res.* **47**, 2455 (2008).
- [47] A. Samanta, Role of slip on the linear stability of a liquid flow through a porous channel, *Phys. Fluids* **29**, 094103 (2017).
- [48] A. Samanta, Linear stability of a plane Couette-Poiseuille flow overlying a porous layer, *Int. J. Multiphase Flow* **123**, 103160 (2020).
- [49] P. G. Drazin and W. H. Reid, *Hydrodynamic Stability* (Cambridge University Press, Cambridge, U.K., 1981).
- [50] A. Samanta, Spatiotemporal instability of an electrified falling film, *Phys. Rev. E* **93**, 013125 (2016).
- [51] P. M. J. Trevelyan and S. Kalliadasis, Wave dynamics on a thin-liquid film falling down a heated wall, *J. Eng. Math.* **50**, 177 (2004).
- [52] J. R. A. Pearson, On convection cells induced by surface tension, *J. Fluid Mech.* **4**, 489 (1958).
- [53] P. Schmid and D. Henningson, *Stability and Transition in Shear Flows* (Springer, Berlin, 2001).
- [54] A. Samanta, Shear wave instability for electrified falling films, *Phys. Rev. E* **88**, 053002 (2013).
- [55] A. Pearlstein, Effect of rotation on the stability of a doubly diffusive fluid layer, *J. Fluid Mech.* **103**, 389 (1981).
- [56] A. C. Or, Finite-wavelength instability in a horizontal liquid layer on an oscillating plane, *J. Fluid Mech.* **335**, 213 (1997).
- [57] A. Samanta, Effect of electric field on an oscillatory film flow, *Phys. Fluids* **31**, 034109 (2019).
- [58] A. Samanta, Modal analysis of a viscous fluid falling over a compliant wall, *Proc. R. Soc. A* **477**, 20210487 (2021).
- [59] U. Lange, K. Nandakumar, and H. Raszillier, Symbolic computation as a tool for high-order long-wave stability analysis of thin film flows with coupled transport processes, *J. Comput. Phys.* **150**, 1 (1999).
- [60] S. Pal and A. Samanta, Linear stability of a surfactant-laden viscoelastic liquid flowing down a slippery inclined plane, *Phys. Fluids* **33**, 054101 (2021).